Dampening effect of global flows on Rayleigh-Taylor instabilities: Implications for deep-mantle plume vis-à-vis hotspot distributions

Arnab Roy, Dip Ghosh and Nibir Mandal

Department of Geological Sciences, Jadavpur University
Kolkata 700032, India

Summary

It is a well-accepted hypothesis that deep-mantle primary plumes originate from a buoyant boundary layer at the Core-Mantle Boundary (CMB), where Rayleigh–Taylor (RT) instabilities play a key role in the plume initiation process. Combining 2D computational fluid dynamic (CFD) model simulations and a linear stability analysis, this article explores how a horizontal global flow in the mantle can influence the growth dynamics of RT instabilities in the source layer. Both the CFD simulation results and analytical solutions predict the global flows as a dampening factor to reduce their growth rates. It is found that layer-parallel global flow velocities (normalized to buoyancy driven upward flow velocity), $U^* > 30$ completely suppress gravitational instabilities on short as well as long wavelengths, and force the entire system to advect in the horizontal direction. We present a series of real-scale numerical simulations to demonstrate the effects of Atwood number (A_T) and the normalized source-layer viscosity (μ^*) on the growth rate of instabilities in a source layer. Decreasing A_T or increasing μ^* significantly reduces the growth rates of the fastest rising plumes. The stability analysis predicts a linear increase of the instability wavelength with the global flow velocity, implying that the plume frequency would drop in kinematically active mantle regions. From this analysis we also show the effects of additional physical parameters: source-layer viscosity and thickness on the growth rate of RT instabilities. The article finally addresses the problem of unusually large inter-hotspot spacing in the light of our CFD simulation results and theoretical solutions, and proposes a new conceptual framework for the origin of sporadically distributed hotspots of deep-mantle sources.

1. Introduction

Rayleigh-Taylor (RT) instability, primarily driven by gravitational forces in an inverted density stratification (i.e., a heavy fluid resting upon a relatively light fluid), governs a wide range of atmospheric and oceanic processes, e.g., global air circulation, cloud formation, oceanic currents as well as many interstellar, and planetary phenomena, e.g., supernova explosion and silicate-metal segregation. Lord Rayleigh and G.I. Taylor first predicted the RT instability growth rate from a linear stability analysis, considering the effects of inertial and body forces between two immiscible inviscid fluids (Rayleigh 1882, Taylor 1950). Since then, the RT theory continued to proliferate in diverse directions with addition of more and more physical variables with time, like surface tension (Pullin 1982, Mikaelian 1996), density gradient (Munro 1988, Song *et al.* 2021), diffusion (Masse 2007), temperature gradient and mass transfer (Gerashchenko & Livescu 2016), effect of rotation (Baldwin *et al.* 2015) and magnetic field (Zrnić & Hendricks 2003). A group of these variables (density gradient, temperature gradient, mass transfer, and diffusion) facilitates the growth of instabilities, whereas another group (surface tension, magnetic field, and rotational forces), in contrast, acts as dampening factors. A complete RT theory thus demands an account of both the driving and dampening factors to predict the dynamics of such gravitational instabilities in natural systems as well as practical applications. The RT instability mechanics has been extensively used in solid earth sciences to conceptualize many important geodynamic processes (Turcotte & Schubert 2002), such as salt dome formation in sedimentary basins (Ramberg 1968a, b, 1972, Miller & Behn 2012), magma transport (Whitehead 1986, Wilcock & Whitehead 1991), intraplate orogenic collapse (Neil & Houseman 1999), downwelling at the lithospheric base (Conrad & Molnar 1997, Houseman & Molnar 1997), silicate mantle-metallic core segregation in the Earth (Ida *et al.* 1987, Mondal & Korenaga 2018). The success of these applications has greatly widened the research scope of mantle dynamics in the light of gravitational instabilities.

Plume formation is recognized as the most effective geodynamic process to drive focused upwelling in Earth’s mantle, and it is a well-accepted hypothesis that they originate mostly from RT instabilities in the thermal boundary layer (TBL) at the core-mantle boundary (CMB) (W. Jason Morgan 1972, Nolet *et al.* 2007, Burke *et al.* 2008, Styles *et al.* 2011) and other regions at relatively shallower depths, such as melt-rich zones above sinking slabs in subduction zones (Gerya & Yuen 2003, Ghosh *et al.* 2020) and transition zones (Brunet & Yuen 2000, Kumagai *et al.* 2007). Plumes initiated by instabilities in the TBL ascend under buoyancy forces of their large heads (~500 to >1000 km in diameter), which trail into narrow tails (~100 to 200 km in diameter). Scaled laboratory experiments and numerical simulations have provided significant insights into their ascent behaviour. Jellinek et al. (2002) demonstrated from analogue experiments that, under a thermal equilibrium condition the dynamic topography formed as a consequence of RT instabilities in the TBL determines the relative spacing of upwelling zones. Similar laboratory experiments showed entrainment of surrounding materials by the bulbous plume heads during their ascent (van Keken et al., 1997). Several experimental studies have reported the transient behaviour of thermal plumes (Davaille & Vatteville 2005) and their geometrical asymmetry as a function of source-layer inclination (Dutta *et al.* 2016). On the other direction, the approach of computational fluid dynamics (CFD) simulations, based on multiphase flow modelling has set a new ground for plume research to deal with complex ascent dynamics due to the interplay of multiple physical factors, e.g., viscoplastic rheology in the lower mantle (Davaille et al. 2018). A number of CFD models, both 2D and 3D, have shown the dynamics of thermal plume initiation from the D" layer in Earth’s mantle (Montague & Kellogg 2000 , Jones et al. 2016, Li & Zhong 2017, Frazer & Korenaga 2022).

To tackle the problem of mantle plume generation, most of the earlier (experimental, theoretical and numerical) studies discussed above conceptualized the plume models within a framework of RT instability theory applicable for stratified fluid systems initially under rest condition (Jellinek & Manga 2004). The overlying heavy fluid chosen to represent the mantle in these models is set to flow entirely under the destabilizing gravity effect of inverted density stratification. However, the assumption of an initially rest kinematic state is hardly valid in Earth's interior because the mantle regions are inherently under the influence of large-scale global flows that originate from various geodynamic processes (Fig. 1), such as down-going slab movement, lithospheric plate motions, global convection and mantle winds (Bekaert *et al.* 2021). Plumes, irrespective of their thermal or thermo-chemical origin, therefore, evolve through kinematic interactions with the ambient mantle flows. However, how global mantle flows can modulate their ascent behaviour is still not well understood. Some workers (e.g., Korenaga 2005) have claimed that mantle plumes remain fixed in their spatial positions despite an active background flow in the mantle. They have supported their claim with seismic images of deep-mantle plumes. Another school holds a completely opposite view, claiming that deep-sourced plumes undergo horizontal deflections under the influence of global flows (e.g., Steinberger & O'Connell 1998), which are also demonstrated from laboratory experiments (Griffiths & Richards 1989, Mark A. Richards & Griffiths 1989, Kerr & Mériaux 2004, Kerr *et al.* 2008). However, none of these studies has attempted to address the most critical questions- in what way does a background flow influence the onset of RT instabilities for plume formation, and secondly, does the flow facilitate or dampen the instability growth? These unresolved issues form the central theme of our present article.

Using 2D finite element particle-in-cell numerical method we performed computational fluid dynamics (CFD) simulation experiments to investigate the problem of RT instability growth at the CMB in mantle subjected to a global horizontal flow. The CFD simulations are utilized to explore the existence of a threshold global velocity at which the instability can be completely suppressed, allowing no plume to grow in the buoyant basal layer. We also develop a linear stability analysis to show a dispersion relation of RT instabilities as a function of layer-parallel flow in the overlying mantle and support our findings from the simulations.

2. CFD Modelling

2.1. Model Approach

We model mantle plumes initiated by Rayleigh Taylor Instability (RTI) in a thin (100 km), low-density layer at the mantle base, overlain by a denser layer (2130 km thick mantle) (Fig. 2). The thin layer is chosen to mechanically replicate a buoyant boundary layer (described as *source layer* in the foregoing discussion) at the Core-Mantle boundary (CMB). The source layer faces gravity driven RTI due to density inversion, forming plumes in course of the instability evolution. We develop our CFD modelling in the framework of incompressible Stokes flow mechanics, reducing the mass and momentum conservation equations to;

$$\nabla . u = 0 \tag{1}$$

$$-\nabla P + \nabla .(\mu\left(\nabla u + \nabla^T u\right)) = 0, \tag{2}$$

where, u is the velocity, μ is the viscosity, P is the dynamic pressure, g is the acceleration due to gravity, ρ is the density and $\hat{z}$ is a unit vector in the direction of gravity. The lower-mantle viscosity is assigned a constant average value to simplify the model setup, with an aim to investigate additional effects of global horizontal flows on plume formation in Earth's mantle. The average viscosity represents the layered mechanical structure as a single model layer. Earlier studies provided different estimates for the lower-mantle viscosity, e.g., ~10^{22} Pa s from geoid anomalies (Richards & Hager 1984), slightly higher than 10^{21} Pa s form postglacial rebound (Cathles 1975, Spada *et al.* 1991). Numerical modelling, on the other hand, yields an estimate of ~3×10^{22} Pa s from the slab sinking rates. Considering these estimates, we fixed the average viscosity of the whole lower mantle at 10^{22} Pa s in our model. We, however, varied the source-layer viscosity (μ) in the range 10^{21} to 10^{18} Pa s (Nakada *et al.* 2012) to account for the mechanical effects of various lateral thermal and chemical heterogeneities at the base of lower mantle reported by several workers (Davies *et al.* 2012, Farnetani *et al.* 2018).

To describe the simulation results, we express the source-layer viscosity (μ) in a normalized form, $\mu^* = \frac{\mu_M}{\mu}$, where μ_M is the overlying mantle viscosity. Similarly, their density contrast (buoyancy factor) is non-dimensionalized in terms of Atwood number (A_T), expressed by

$$A_T = \frac{\rho_1 - \rho_2}{\rho_1 + \rho_2} \tag{3}$$

where ρ_1 and ρ_2 are the densities of heavier and lighters fluids. A_T is varied in the range 0.01 to 0.04 (Nipin & Tomar 2015). We also normalize the RTI wavelength (λ) with source-layer thickness (H) as $\lambda^* = \lambda/H$.

We impose a kinematic boundary condition at the upper model boundary to introduce a global flow in the model mantle, which is the prime concern of our present study (Fig. 2). The bottom wall is assigned a no-slip boundary condition, keeping the two side walls under a periodic boundary condition. We used the open-source finite element code of Underworld 2 (http://www.underworldcode.org/) to solve the mass and momentum conservation equations (Eq. 1 and 2) for the CFD simulations. This code works within a continuum mechanics approximation, and has been extensively used to deal with a range of geological and geophysical problems (Mansour *et al.* 2020). As shown by previous workers (Moresi *et al.* 2007, Lemiale *et al.* 2008), the code discretizes the geometrical domain into a standard Eulerian finite element mesh and the domain is coupled with the particle-in-cell approach (Evans *et al.* 1957). This numerical approach is found to be effective to successfully discretize the material domain into sets of Lagrangian material points, which carry material properties that are history-dependent and can be tracked over the entire simulation run. The mass and momentum conservation equations are solved to find the pressure and velocity conditions within the model domain. The physical properties of model materials, such as plume density and viscosity, are mapped using these advection equations through particle indexing.

2.2. Model Results

2.2.1. Dampening effects of horizontal global flows

We systematically increased the top model-boundary velocity (U_o) to evaluate the effect of global flows on the growth rates of instabilities in the source layer (estimated from the vertical ascent-velocity component of instability-driven domes). U_o is non-dimensionalized in terms of the initial accent velocity (v_y), given by Ramberg (1968),

$$\frac{v_y}{\Delta A} = -K\frac{\rho_1 - \rho_2}{2\mu_2}h_2 g, \quad (4)$$

where K is a constant that depends on the viscosity and the wavelength of the system under consideration (details provided in Supplementary S1). ΔA denotes a small initial amplitude of the instability. The non-dimensional boundary velocity, $U^* = U_o / v_y$ was varied in the range 0 to 30 (elaborated in Supplement), keeping A_T and μ^* constant.

The reference experiment run for an initially rest mantle condition ($U^* = 0$) shows that the RT instabilities start to amplify with an appreciable rate (~3 cm/yr) at a model run time, t = ~20 Ma. The instabilities then grow with exponentially increasing rates to form typical plume structures (bulbous heads trailing into narrow tails) at t ~27 Ma (Fig. 3). At this stage, the plume heads ascend vertically through the mantle at the rates of 12 to 15 cm/yr, which closely agree with the Stokes formula (Turcotte and Schubert, 2002). In a simulation with $U^* = 15$ (Fig.S2) the global flow is found to dampen the instability growth in the initial stage, allowing them to grow at a relatively lower rate (~ 2.6 cm/yr) on a longer time scale (t = ~24 Ma), and the fastest growing instabilities attain a typical plume structure at t = ~34 Ma. The dampening effect strengthens further when U^*= 30, where the instabilities grow in amplitude at much slower rates (~ 1 cm/yr at t = ~22 Ma) (Fig. 3) that becomes almost steady with time. Under this kinematic condition the instabilities eventually do not form any typical plume structure even after a very long model run time (t ~ 50 Ma) (Fig. 4).

The CFD simulation results described above clearly suggest that horizontal global flows in the mantle always act as a dampening factor in the RT instability dynamics and suppress the process of plume formation in the basal buoyant layer. Fig 4a and b show reducing plume ascent heights and vertical ascent velocities of the fastest growing instabilities with increasing U^*.

2.2.2. Role of source-layer buoyancy

For low buoyancy (A_T = 0.01), the instabilities start to significantly grow in amplitude (0.3 cm/yr) at t = ~24 Ma, and the fastest growing waves (2 cm/yr) form a typical head-tail structure of the plume at t = ~40 Ma that continued to ascend vertically through the mantle layer. Increase in A_T greatly facilitates the RT instability growth as expected, and develops mature plume structures on much shorter time scales, for example, t = ~13 Ma when A_T = 0.03. For a given simulation run time, the growth rate of instabilities increases with increasing A_T (Fig. 5), but showing little variations in their wavelengths. Fig 7a and b present sets of graphical plots to show temporal variations of the ascent height of the fastest growing plumes and their ascent velocity, respectively as a function of A_T.

2.2.3. Effects of source-layer viscosity

For a high source-layer viscosity (μ^* = 10^{-2}), the instabilities are initiated with a non-dimensional wavelength, λ^* = 12 – 15, and they grow at significant rates (2 cm/yr) on a model run time, t = ~ 20 Ma (Fig. 6) and subsequently give rise to plume structures on a time scale of ~30 Ma. In addition to the fastest growing waves, several secondary waves evolve into plume structures at relatively shorter wavelengths (λ^* = 300 – 400). Lowering in μ^* facilitates the instability growth rates and thereby reduces the time scale of plume formation (Fig. 6). For example, μ^* = 10^{-4} yields fastest growing instabilities at t = ~ 8Ma, which form typical head-tail plume structures within a much shorter time scale (t ~12 Ma). The initial instability wavelengths calculated from these simulations hold an inverse relation with the source-layer viscosity (λ^* = ~5 when μ^* = 10^{-1} to λ^* = ~30 when μ^* = 10^{-4}).

The vertical ascent height of plumes and their corresponding ascent velocities are summarily shown in graphic plots for different μ^* values (Figs. 7c &d). Interestingly, the inverse relations of plume ascent velocity with the source-layer viscosity obtained from our models have been also reported in earlier studies (van Keken *et al.* 1997).

3. Linear stability analysis

3.1. Mathematical formulation

Consider a thin, mechanically distinct layer (source layer) above the CMB, lying below the mantle, subjected to a global horizontal flow, as illustrated in Fig 8. Here we develop the theory based on a thin-layer approximation, which assumes layer thickness (h) much smaller than the length scale of the system (Bredow *et al.* 2017). We choose a Cartesian coordinate system, *xz* with the z axis in the vertical direction (positive upward). The thin layer is confined between two horizontal surfaces: $z = 0$ and $z = h(x,t)$ that represents the interface between the layer and the overlying mantle. The thin layer is assigned a negative density contrast relative to the overlying mantle region, and the entire system rests upon an undeformable substrate. We consider a layer parallel velocity condition at the interface $z = h(x,t)$ that forces materials in the thin layer to advect in the horizontal direction. The linear stability analysis is developed in the framework of mass and momentum conservation conditions, as in the CFD simulations. Considering incompressible fluid in the thin-layer, using Eq. (1) we expand the mass conservation equation as,

$$\frac{\partial v_T}{\partial z} + \frac{\partial u_T}{\partial x} = 0, \tag{5}$$

where u_T and v_T denote the x- and z components of the flow velocity in the thin-layer, respectively. Applying the thin-layer approximation, the momentum conservation conditions follow

$$\frac{\partial p}{\partial z} = -\Delta\rho g \tag{6}$$

and

$$\mu\frac{\partial^2 u_T}{\partial z^2} - \frac{\partial p}{\partial x} = 0, \tag{7}$$

where p is the excess hydrostatic pressure, $\Delta\rho$ is the negative density contrast between the thin-layer and the overlying medium, and μ is the fluid viscosity of the thin layer. The differential equations are solved using a set of boundary conditions (BCs) in the following way. The bottom surface is subjected to an impenetrable boundary condition:

$$v_T|_{z=0} = 0. \tag{8}$$

In addition, assuming a free-slip condition at this boundary, we have

$$\left.\frac{\partial u_T}{\partial z}\right|_{z=0} = 0 \tag{9}$$

The layer-interface, on the other hand, is subjected to a normal stress condition, which is obtained by integrating Eq. (2) in the range 0 to h across the thin layer,

$$p = \Delta\rho g|h - z|_{z=0} + p|_{z=h} \tag{10}$$

where $p|_{z=h}$ is the dynamic pressure at the mantle-thin layer interface and $p|_{z=0}$ is the dynamic pressure at the bottom of the domain. To deal with the mathematical problem, we non-dimensionalize the governing equations and the BCs using the following variables

$$x^* = \frac{x}{L}, z^* = \frac{z}{h}, u_T^* = \frac{u_T\mu}{\Delta\rho g h^2}, v_T^* = \frac{v_T\mu}{\Delta\rho g h^2}. \tag{11}$$

The governing equations then become,

$$\frac{\partial v_T^*}{\partial z^*} + \frac{\partial u_T^*}{\partial x^*} = 0, \tag{12}$$

$$\frac{\partial p}{\partial z^*} = -\Delta \rho g \tag{13}$$

$$\mu \frac{\partial^2 u_T^*}{\partial z^{*2}} - \frac{\partial p}{\partial x^*} = 0, \tag{14}$$

and the BCs reduce to

$$v_T^* |_{z^*=0} = 0 \tag{15}$$

$$\left.\frac{\partial u_T^*}{\partial z^*}\right|_{z^*=0} = 0 \tag{16}$$

$$p = \Delta \rho g |h - z^* |_{z^*=0} + p|_{z^*=1} \tag{17}$$

To ease the mathematical expressions, we will omit the asterisk symbol now and onward. To derive the horizontal velocity component in the thin layer, substituting Eq. (17) in Eq. (14), we have

$$\mu \frac{\partial^2 u_T}{\partial z^2} - \frac{\partial}{\partial x}(\Delta \rho g h + p|_{z=1}) = 0 \tag{18}$$

On integration and after applying the boundary conditions (Eq. 15, 16), the differential equation (Eq. 18) yields

$$u_T = u_T|_{z=1} + \frac{1}{2\mu} \frac{\partial}{\partial x}(\Delta \rho g h + p|_{z=1})(z^2 - h^2) \tag{19}$$

The corresponding vertical component is derived from the mass conservation equation (Eq. 12) after applying the impenetrable BC at $z = 0$ (Eq. 15) as,

$$v_T|_{z=1} = u_T|_{z=1} \frac{\partial h}{\partial x} - \frac{\partial}{\partial x} \int_0^1 u_T dz \tag{20}$$

Substituting Eq. 19 into this equation, we get

$$v_T|_{z=1} + h \frac{\partial u_T|_{z=1}}{\partial x} - \frac{\partial}{\partial x}\left[\frac{h^3}{3\mu} \frac{\partial}{\partial x}(\Delta \rho g h + p|_{z=1})\right] = 0 \tag{21}$$

Considering the kinematic boundary condition at the interface,

$$\frac{\partial h}{\partial t} = v_T\big|_{z=1} - u_T\big|_{z=1}\frac{\partial h}{\partial x}, \tag{22}$$

Eq. 21 yields,

$$\frac{\partial h}{\partial t} + \frac{\partial}{\partial x}\left(hu_T\big|_{z=1}\right) - \frac{\partial}{\partial x}\left[\frac{h^3}{3\mu}\frac{\partial}{\partial x}\left(\Delta\rho g h + p\big|_{z=1}\right)\right] = 0. \tag{23}$$

Eq. 23 defines the evolution of the interface, governed by the two competing forces: 1) non-hydrostatic pressure forces arising from the negative density contrast between the thin-layer and the mantle (3rd term) and 2) viscous forces due to the layer-parallel advective flow at the interface (2nd term). We now introduce a horizontal velocity at the interface as

$$u_T\big|_{z=1} = u_M\big|_{z=1} = U(x,t) \tag{24}$$

It is to note that the overlying horizontal mantle flows can be perturbed at some incipient geometrical irregularities on the thin layer, producing spatially and temporally heterogeneous layer-parallel flows close to the interface, as revealed from numerical simulations (Fig S3). We thus generalize this theoretical problem by setting the boundary condition $u_T\big|_{z=h}$ as a function of *x* and *t*.

The vertical flows in the basal layer develop pure shear components at the interface, the rate of which can be expressed as (Hernlund et al., 2018),

$$\dot{\epsilon} = -\left(\frac{\partial v}{\partial z}\right)\bigg|_{z=0}. \tag{25}$$

The corresponding dynamic pressure at the interface follows,

$$p\big|_{z=1} = \mu_M\dot{\epsilon}, \tag{26}$$

The boundary condition (Eq. 24) represents a heterogeneous horizontal mantle flow condition as a function of *x* on the layer interface at a given instant. We choose a sine wave function with a characteristic wavenumber k_M and a characteristic length-scale L to express the spatially varying horizontal interfacial flows. We later show the linear stability analysis in the perspective of different k_M versus k (instability wavelength) relations. Now, using the continuity equation (Eq. 12) in Eq. 25, the expression of strain rate at the interface follows,

$$\dot{\epsilon} = -\frac{u_M|_{z=1} k_M}{2} \cos\left(\frac{k_M x}{2}\right) \tag{27}$$

By combining Eqs. 23, 26 and 27, we obtain the final equation that expresses the geometrical evolution of the interface between the basal thin layer and the overlying mantle in the presence of a global horizontal flow:

$$\frac{\partial h}{\partial t} + \frac{\partial}{\partial x}(h u_T|_{z=1}) - \frac{\partial}{\partial x}\left[\frac{h^3}{3\mu}\frac{\partial}{\partial x}\left(\Delta\rho g h - \mu_M \frac{U_0 k_M}{2} \cos\left(\frac{k_M x}{2}\right)\right)\right] = 0, \tag{28}$$

where U_0 stands for the maximum horizontal flow magnitude at the interface, determined by the global horizontal flow velocity in the overlying mantle. At infinitesimal time the interfacial deflection (h_d) is assumed to be small enough such that $h_d \ll \varepsilon h$. Under this condition the linear terms determine the growth of instabilities at the interface in the system. The first term within the third bracket in Eq. (28) represents the favoring force, where the density difference ($\Delta\rho$) facilitates the low-density fluid in the thin-layer to push vertically up against the overlying denser mantle. On the other hand, the second term represents the dynamic pressure at the interface set by the large-scale horizontal flow that tends to dampen the instability growth under the boundary condition within the characteristic length (L).

To derive the dispersion relation of an instability at the interface, we introduce a small perturbation to the mean height of the interface,

$$h(x,t) = h_0 + \varepsilon h_d(x,t), \tag{29}$$

where h_0 is the mean height of the interface and $h_d(x,t)$ represents the perturbation with $\varepsilon \ll 1$. Using Eq. (29) in Eq. (28) and keeping only the $O(\varepsilon)$ terms, we find

$$\frac{\partial h_d}{\partial t} + \frac{\partial}{\partial x}(h_d u_T|_{z=1}) - \frac{\partial}{\partial x}\left[\frac{h_0^3}{3\mu}\Delta\rho g \frac{\partial h_d}{\partial x} - \frac{\mu_M h_0^2 h_d U_0 k_M}{\mu \quad 2} \cos\left(\frac{k_M x}{2}\right)\right] = 0 \tag{30}$$

Note that any perturbation developed at the interface will simultaneously advect in the x-direction in response to the layer-parallel mantle flow. We thus choose a spatio-temporal perturbation in the following form:

$$h_d(x,t) = A\exp i(kx - \omega t), \tag{31}$$

where A is a pre-factor, k is the perturbation wavenumber, and ω is the angular frequency. Substituting the expression of $h_d(x,t)$ in Eq. (30), and after some algebraic manipulation, we get

$$\omega = ku_T\big|_{z=1} - i\frac{\partial u_T\big|_{z=1}}{\partial x} + i\frac{h_0^3}{3\mu}\Delta\rho g k^2 + i\frac{h_0^2 k_M^3 U_0 \mu_M}{8\mu}\cos\left(\frac{k_M x}{2}\right) - \frac{h_0^2 k_M^2 k U_0 \mu_M}{4\mu}\sin\Bigg(\quad (32)$$

This equation provides a dispersion relation for interfacial instability in a complex form. Its imaginary part yields the growth rate as,

$$\sigma = -\frac{\partial u_T\big|_{z=1}}{\partial x} + \frac{h_0^3}{3\mu}\Delta\rho g k^2 + \frac{h_0^2 k_M^3 U_0 \mu_M}{8\mu}\cos\left(\frac{k_M x}{2}\right) \tag{33}$$

Considering the mantle advection model, this equation takes the following form.

$$\sigma = \frac{k_M U_0}{2}\cos\left(\frac{k_M x}{2}\right) + \frac{h_0^3}{3\mu}\Delta\rho g k^2 + \frac{h_0^2 k_M^3 U_0 \mu_M}{8\mu}\cos\left(\frac{k_M x}{2}\right) \tag{34}$$

3.2. Analytical results

We will now use Eq. 34 to study the effects of model parameters on the growth rate (σ^*) of Rayleigh-Taylor instabilities in the thin layer. We first undertake this study for a condition of comparable k_M and k values ($k_M \sim k$), i.e., the length-scale of horizontal flow heterogeneity at the layer interface is close to that of instabilities growing in the thin-layer. The analysis is then extended for a condition, $k_M \ll k$, which implies the horizontal flow heterogeneity far exceeding the instabilities in length scales. For $k_M \sim k$, increasing U_0^* (a non-dimensional form of U_0) facilitates the system to become more stable, as reflected from reducing amplitudes of the dispersion curve in Figure S4. U_0^* also greatly influences the wavenumber (k) corresponding to the most unstable modes, forming an inverse relation of k with U_0^*. For example, k = 0.5 for U_0^* = 10, which drops to nearly 0.2 at U_0^* = 30. The theoretical results (Fig 9a) suggest that increasing horizontal flow velocity in the mantle favours interfacial instabilities to grow at longer wavelengths, and at the same time dampens their growth rates.

We now consider the second case, $k_M \ll k$ to show the effects of U_0^* on the modes of instability growth in the thin layer from two graphical plots for U_0^* = 20 and 30. We compare these plots with those for $k_M = k$ to find additional influence of the k_M versus k relation. Increase in U_0^* yields similar inverse impacts on both the maximum growth rates and their corresponding wave numbers, irrespective of $k_M \ll k$ or $k_M = k$ conditions. However, for a given U_0^* a transition from $k_M \ll k$ (Fig. S4a, dashed lines) to $k_M = k$ (Fig. 9a) condition greatly reduces the dominant wavenumber and its corresponding growth rate, implying that the latter condition is less effective to produce instabilities in the basal thin layer.

The non-dimensional source-layer viscosity (μ) is another influential factor for the dispersion of various modes, as shown from a set of graphical plots in Figure 9b. For a given U_0 and h_0, the plots indicate that increasing μ while keeping the overburden layer viscosity (μ_M) constant, significantly dampens the growth rate of the RTIs (Fig. 9b, black and red lines). The instabilities which grow against the prevalent gravitational forces, undergo significantly more resistance for higher values of source-layer viscosity, leading to the observed dampening effect of μ. (Fig. 9b, blue, green lines). We also investigated the effects of source-layer viscosity for the two conditions: $k_M = k$ and $k_M \ll k$ (Fig. S4b). For a given source layer viscosity, μ, a change in the condition from $k_M = k$ and $k_M \ll k$ reduces the amplitude (maximum growth rate) of dispersion relations and their corresponding wavenumbers (Fig. S4b, dashed lines).

Using Eq. 34 we studied the evolution of interfacial instabilities as a function of the initial layer thickness (h_0). Increasing h_0 facilitates their growth rate because the destabilizing force (second term in the equation) is proportional to h_0^3. For extremely thin layers (low value of h_0), the long waves remain marginally stable or unstable. The short waves, in contrast, are always stabilized, primarily due to viscous effects of the thin-layer (Fig. S5a). Unlike the previous factors, increasing h_0 decreases the wavenumber corresponding to the most dominant mode that agrees well with the common observation that the wavelength of instabilities holds a positive correlation with layer thickness. For a given $h_0$value, a switch over in the condition from $k_M = k$ to $k_M \ll k$ promotes the destabilizing state in the system (Fig. S5b, dashed lines) both in terms of increasing growth rate and wavenumber (i.e., reducing wavelength).

4. Discussions

4.1. RTI simulations and theoretical predictions: a synthesis

This study primarily shows that an interface-parallel velocity in horizontally stratified fluid layers of inverted densities results in significant dampening of the RT instabilities in the layered systems, where their growth rate is found to be inversely related to the interface-parallel velocity magnitude (U^*). Our CFD simulations suggest that $U^* \geq 15$ can noticeably dampen them, and $U^* > 30$ completely arrests the RT instabilities to amplify into a plume structure (Fig. 4a, b). The theoretical results also predict from the linear stability analysis that strong global flows significantly dampen the growth of instabilities. For low layer-parallel velocities (U_0^* ~10), such ambient flows dampen preferentially the shortwave instabilities (i.e., of higher wavenumbers); in contrast, for high layer-parallel velocities ($U_0^* \geq 20$) they affect both the short as well as the long waves (Fig. 9a). However, ambient velocity fields, in general, facilitate RT instabilities to grow on longer wavelengths in preference to those on shorter wavelengths (Fig. 9a). The theoretical prediction implies that the ambient mantle flows reduce the spatial frequency of plumes, allowing them to form at a large horizontal spacing, as reflected in the sporadic distributions of plume-driven hotspots (discussed in detail later).

We dealt with the Atwood number (A_T) in our CFD simulations, aiming to evaluate the effects of density contrast ($\Delta\rho = \rho_m - \rho_p$) between the source layer and the overlying mantle. The density contrast is an important factor in the context of our present problem as the lower mantle is compositionally as well thermally heterogeneous (Davies *et al.* 2012, Farnetani *et al.* 2018), and such heterogeneities can eventually give rise to a large spatial variation in $\Delta\rho$. The simulation results yield a positive relation of the instability growth rate with density ratio, as also predicted by earlier studies (van Keken *et al.* 1997) as well as our present stability analysis (Fig. 5). Increasing density ratio facilitates instabilities to amplify at fast rates (Fig. 7a, b). This finding allows us to hypothesize that inherent heterogeneities can be an important factor in preferential growth of mantle plumes initiated by RT instabilities. Thermo-chemical heterogeneities in mantle, e.g., TBL piling, can also result in lateral variations of the mantle viscosity, as reported from seismic tomographic studies (McNamara & Zhong 2004, Davaille & Romanowicz 2020). Our analytical solution shows that for a constant source-layer viscosity, the wavelength of RT instabilities increases linearly with the overlying mantle viscosity (Fig. 10b). The theoretical result implies that the number of possible plumes in a region of high mantle-viscosity would be low, but they will grow at fast rates.

4.2. Impact of global flows on RT instability: geodynamic perspectives

Earlier theoretical and experimental studies showed the evolution of mantle plumes originated from deep mantle sources by RT instabilities. However, most of these studies considered the initial kinematic state of mantle in rest condition, which is hardly applicable to the actual mantle system as a number of thermal as well as mechanical processes, such as thermal convection (Olson *et al.* 1990), subducting slab driven shear flows (Čížková *et al.*

2012, van der Meer *et al.* 2018), and mantle winds set in large-scale horizontal flows (Fig. 1). Model estimates suggest that subducting slabs sink in the lower mantle with velocity magnitudes in the range 4 -5 cm/yr at the top to 2-3 cm/yr at the bottom, whereas the maximum root-mean-square vector velocity field for whole mantle convection is estimated around 30 cm/year (Rayleigh number in the order of 10^6). Our reference CFD simulation ($U^* = 0$) provides an estimate of 1 – 2 cm/yr for the initial growth rate of instabilities in the source layer. The global ambient flows in the overlying mantle can thus greatly influence the process of plume initiation at the TBL. In fact, some model studies have recently shown that such global flows can force ascending plumes to deflect from the vertical trajectories (Kerr & Mériaux 2004, Kerr *et al.* 2008, Hassan *et al.* 2016), as documented from the seismic tomography of natural plumes, e.g., the Hawaiian plume is strongly deflected towards the west–southwest at around 1000 km depth (French & Romanowicz 2015, Lei *et al.* 2020). However, these studies entirely focus on the interaction of mature plumes with global horizontal flows, giving little attention to the problem of plume initiation in a source layer, which fundamentally determines the possibility of plume formation in a geodynamic setting. The linear stability analysis also suggests that the horizontal global flows in the mantle can critically control the initiation of plume instabilities in buoyant source layers. In extreme conditions they can completely suppress the instabilities, allowing no plume to evolve in the system. For a mechanical setting with $A_T = 0.01$ and $\mu^* = 10^{-1}$, instabilities that can amplify at a velocity of ~0.3-0.5 cm/yr in a rest mantle condition, are effectively suppressed as the mantle flows attain a threshold condition ($U^* \geq 30$, i.e., 10-15 cm/yr in the absolute scale). This RT instability mechanics is applicable to several other geodynamic settings, which is briefly discussed below.

Subduction zones are a typical geodynamic setting that commonly produce plumes, called cold plumes, initiated as RT instabilities in the buoyant melt-rich zones above the subducting slabs (Gerya & Yuen 2003, Ghosh *et al.* 2020). In this setting the subducting slabs typically set in a strong corner flow currents with appreciable magnitudes ($\sim 5 - 10$ cm/yr), depending upon the subduction velocity that generally varies on a wide spectrum ($4 - 20$ cm/yr). Applying our model results, we suggest that strong slab-parallel advection in the mantle wedge can dampen the RT amplification in the vertical direction, allowing those with high buoyancy factor to preferentially take part in instability driven plume generation. The transition zone (670 km) is another effective geodynamic setting for secondary plume formation from mega plumes, often stagnated at the transition zone (Brunet & Yuen 2000). Many thermo-mechanical models and experiments indicate that the overlying lithospheric plate motion can globally induce horizontal flows in the upper mantle, where their magnitudes can be significantly large (8-10 cm/yr). According to our model results, such lithosphere-induced flows counter to the destabilizing condition at the transition zone, reducing the possibility of plume formation. This model inference is also applicable for secondary plume generation from a super-plume beneath a drifting continental lithosphere, where the lithospheric motion can greatly suppress the RT instabilities in the melt-rich layers at the top of the super-plume.

4.3. Magmatic hotspots on Earth's surface: some questions

Morgan (1971) in his seminal work proposed deep-mantle plumes as the principal source of primary magmatic hotspots, but their origin has remained a subject of great debate till date (Koppers *et al.* 2021). Later studies proposed a set of criteria in support of the deep-mantle hypothesis for hotspots: a) linear chain of volcanoes with monotonous age progression, b) flood basalt at the origin of this track, c) a large buoyancy flux, d) the presence of consistently high ratios of three to four helium isotopes, and e) occurrence of low shear-wave velocity (V_S) zones in the lower mantle. Based on these criteria, it has been possible to ascertain the following nine hotspots of deep-mantle origin: Hawaii, Pitcairn, Samoa and Louisville (Jellinek & Manga 2004, Koppers *et al.* 2021) in the Pacific hemisphere and Iceland, Afar, Reunion, Tristan and Kerguelen in the Indo-Atlantic hemisphere (Fig. 11). Their spatial distribution reveals that these hotspots are located at large distances from one another. For example, the Hawaii chain and the Samoan hotspot are located ~5000 km away from each other. Similarly, the Iceland and the Tristan hotspots maintain a spacing, more than 8000 km. On contrary, experimental and theoretical studies (Montague & Kellogg 2000) show mantle plumes generated in the TBL at the CMB at much smaller wavelengths, lying in the range 1400 km to 1800 km. The plume frequency observed in experimental models evidently holds a clear disagreement with the spatial density of deep-mantle hotspots across the globe. This disagreement poses the following critical question- why are hotspots of deep-mantle plume origin so rare on the earth's surface?

One of the reasonable ways to address this question is to find some geodynamic processes that can inhibit plume initiation in the TBL above the CMB, allowing a few plumes to grow in the mantle and produce sporadic hotspots. The present article identifies global horizontal mantle flows as one of the potential dampening factors for mantle plume generation. The linear stability analysis shows that the RT instability growth rate becomes negligibly small (s ~ 0) when the interface parallel flow velocity is significant ($U^* = \sim 20$). The same global flow effect is observed in the real scale CFD simulations, where the growth rate drops significantly due to imposition of a global flow $U^* = >15$ (Fig. 3b). The simulation results imply that mantle plumes to ascend to the surface in the flowing mantle states would require an unusually large time scale (~>100 Ma). The mantle flows can also control their spatial frequency, as revealed from the instability wavenumber (k) analysis as a function of U_0 (Fig.11a). k corresponding to the fastest growing waves is reduced with increasing U_0. Applying this theoretical result to a real scale system, it appears that the wavelength of instabilities in a layer of 100 km thickness would be ~250 km in case of rest mantle condition, which multiplies by 10-14 times when the mantle is subjected to a global flow condition of 5 cm/yr. Our instability theory thus provides at least a clue to the problem of large spacing, i.e. low frequency of volcanic hotspots in the light of RT instability mechanics.

4.4. Model limitations

Both the numerical models and the theory presented in this article have a number of limitations. 1) Both of them are developed in the framework of a mechanical approach, without considering the thermal effects. This assumption was adopted to focus upon the ambient mantle flows as the factor of our main concern in the analysis of RT instabilities. Evidently, there is a need to widen the scope of this study to investigate the additional effects of temperature on the plume growth. 2) This study also excludes the possible effect of rheological stratification in the mantle and depth-dependent mineral phase transformations. 3) The theory linearizes the problem, excluding the non-linear terms. This approach limits us from performing an analysis for time dependent plume growth. Secondly, the theory predicts the instability wavelength being not sensitive to source-layer viscosity. In contrast, the CFD models show a clear correlation between them. This difference possibly results from the thin-layer approximation chosen in the theory. Finally, the present theoretical formulation excludes complex processes, such as piling at TBL, as shown by previous workers (Heyn *et al.* 2018).

5. Summary and conclusions

This article reports the role of horizontal global flows in controlling RT instabilities in a buoyant source layer beneath a heavier fluid medium, and addresses the problem of plume formation in the TBL above the CMB earth's mantle. Combining CFD simulation results with a linear stability analysis, this study finally leads to the following conclusions. 1) The global flows always have dampening effects on the growth of RT instabilities. Flow velocities with magnitudes nearly 30 times the initial plume accent velocity impedes the instability to grow into a characteristic plume structure. 2) The linear stability analysis confirms the dampening effects of global flow velocity on the instability growth, where the layer-parallel mantle flow > 30 times that of the vertical component of initial plume growth effectively affect short as well as almost all long-wave instabilities. Moreover, we show that with increasing ambient velocity, the dominant instability wavelength increases by 10 to 40 times the initial layer thickness as the normalized layer parallel velocity is increased from 10 to 30. 3) The theory also predicts the effects of additional factors: density ratio, source-layer viscosity and layer thickness on the growth rate of an instability in an RTI system. All the three physical parameters act as a driving role in facilitating the instability growth rate. 4) The dampening effects of global flows established in this study can explain the mechanics of plume generation in various geodynamic settings, such as subduction zones and the 670 km transition zone. Finally, the theory provides a potential explanation for spatially distant primary mantle plumes, manifested in the form of a few hotspots on earth's surface.

Acknowledgements

A.R. gratefully acknowledges CSIR, India for awarding research fellowship grants (09/096(0940)/2018- EMR-I) and D. G. acknowledges UGC for Senior Research Fellowship. This work used the ARCHER2 UK National Supercomputing Service (https://www.archer2.ac.uk). The DST-SERB is acknowledged for supporting this work through the J.C. Bose fellowship (SR/S2/JCB-36/2012) to N.M.

Data accessibility

The open-source geodynamic code Underworld is available at http://www.underworldcode.org, and model parameters required to replicate the results are detailed in the manuscript.

References

Baldwin, K.A., Scase, M.M. & Hill, R.J.A. (2015) The inhibition of the Rayleigh-Taylor instability by rotation. *Sci Rep*, **5**, Nature Publishing Group. doi:10.1038/srep11706

Bekaert, D. v., Gazel, E., Turner, S., Behn, M.D., Moor, J.M. de, Zahirovic, S., Manea, V.C., *et al.* (2021) High 3He/4He in central Panama reveals a distal connection to the Galapagos plume. *Proc Natl Acad Sci U S A*, **118**, e2110997118, National Academy of Sciences. doi:10.1073/PNAS.2110997118/SUPPL_FILE/PNAS.2110997118.SD03.XLSX

Bredow, E., Steinberger, B., Gassmöller, R. & Dannberg, J. (2017) How plume-ridge interaction shapes the crustal thickness pattern of the Réunion hotspot track. *Geochemistry, Geophysics, Geosystems*, **18**, 2930–2948. doi:10.1002/2017GC006875

Brunet, D. & Yuen, D.A. (2000) Mantle plumes pinched in the transition zone. *Earth Planet Sci Lett*, **178**, 13–27, Elsevier. doi:10.1016/S0012-821X(00)00063-7

Burke, K., Steinberger, B., Torsvik, T.H. & Smethurst, M.A. (2008) Plume Generation Zones at the margins of Large Low Shear Velocity Provinces on the core–mantle boundary. *Earth Planet Sci Lett*, **265**, 49–60, Elsevier. doi:10.1016/J.EPSL.2007.09.042

Cathles, L.M. (1975) The viscosity of the earth's mantle. *Published in **1975** in Princeton NJ) by Princeton university press*, 413, Princeton (N.J.) : Princeton university press, 1975. Retrieved from https://lib.ugent.be/catalog/rug01:001350016

Čížková, H., Berg, A.P. van den, Spakman, W. & Matyska, C. (2012) The viscosity of Earth's lower mantle inferred from sinking speed of subducted lithosphere. *Physics of the Earth and Planetary Interiors*, **200–201**, 56–62, Elsevier. doi:10.1016/J.PEPI.2012.02.010

Conrad, C.P. & Molnar, P. (1997) The growth of Rayleigh-Taylor-type instabilities in the lithosphere for various rheological and density structures. *Geophys J Int*, **129**, 95–112, Oxford University Press. doi:10.1111/J.1365-246X.1997.TB00939.X

Courtillot, V. & Olson, P. (2007) Mantle plumes link magnetic superchrons to phanerozoic mass depletion events. *Earth Planet Sci Lett*, **260**, 495–504, Elsevier. doi:10.1016/J.EPSL.2007.06.003

Davaille, A., Carrez, P. & Cordier, P. (2018) Fat Plumes May Reflect the Complex Rheology of the Lower Mantle. *Geophys Res Lett*, **45**, 1349–1354, John Wiley & Sons, Ltd. doi:10.1002/2017GL076575

Davaille, Anne & Romanowicz, B. (2020) Deflating the LLSVPs: Bundles of Mantle Thermochemical Plumes Rather Than Thick Stagnant "Piles". *Tectonics*, **39**, e2020TC006265, John Wiley & Sons, Ltd. doi:10.1029/2020TC006265

Davaille, Anne & Vatteville, J. (2005) On the transient nature of mantle plumes. *Geophys Res Lett*, **32**, 1–4, John Wiley & Sons, Ltd. doi:10.1029/2005GL023029

Davies, D.R., Goes, S., Davies, J.H., Schuberth, B.S.A., Bunge, H.P. & Ritsema, J. (2012) Reconciling dynamic and seismic models of Earth's lower mantle: The dominant role of thermal heterogeneity. *Earth Planet Sci Lett*, **353–354**, 253–269, Elsevier. doi:10.1016/J.EPSL.2012.08.016

Dutta, U., Baruah, A. & Mandal, N. (2016) Role of source-layer tilts in the axi-asymmetric growth of diapirs triggered by a Rayleigh–Taylor instability. *Geophys J Int*, **206**, 1814–1830, Oxford Academic. doi:10.1093/GJI/GGW244

Evans, M., Harlow, F. & Bromberg, E. (1957) The Particle-In-Cell Method for Hydrodynamic Calculations. Retrieved from https://apps.dtic.mil/sti/citations/ADA384618

Farnetani, C.G., Hofmann, A.W., Duvernay, T. & Limare, A. (2018) Dynamics of rheological heterogeneities in mantle plumes. *Earth Planet Sci Lett*, **499**, 74–82, Elsevier B.V. doi:10.1016/j.epsl.2018.07.022

Frazer, W.D. & Korenaga, J. (2022) Dynamic topography and the nature of deep thick plumes. *Earth Planet Sci Lett*, **578**, Elsevier B.V. doi:10.1016/j.epsl.2021.117286

French, S.W. & Romanowicz, B. (2015) Broad plumes rooted at the base of the Earth's mantle beneath major hotspots. *Nature 2015 525:7567*, **525**, 95–99, Nature Publishing Group. doi:10.1038/nature14876

Gerashchenko, S. & Livescu, D. (2016) Viscous effects on the Rayleigh-Taylor instability with background temperature gradient. *Phys Plasmas*, **23**, 072121, AIP Publishing LLCAIP Publishing. doi:10.1063/1.4959810

Gerya, T. v. & Yuen, D.A. (2003) Rayleigh–Taylor instabilities from hydration and melting propel 'cold plumes' at subduction zones. *Earth Planet Sci Lett*, **212**, 47–62, Elsevier. doi:10.1016/S0012-821X(03)00265-6

Ghosh, D., Maiti, G., Mandal, N. & Baruah, A. (2020) Cold Plumes Initiated by Rayleigh-Taylor Instabilities in Subduction Zones, and Their Characteristic Volcanic Distributions: The Role of Slab Dip. *J Geophys Res Solid Earth*, **125**, Blackwell Publishing Ltd. doi:10.1029/2020JB019814

Griffiths, R.W. & Richards, M.A. (1989) The adjustment of mantle plumes to changes in plate motion. *Geophys Res Lett*, **16**, 437–440, John Wiley & Sons, Ltd. doi:10.1029/GL016I005P00437

Hassan, R., Müller, R.D., Gurnis, M., Williams, S.E. & Flament, N. (2016) A rapid burst in hotspot motion through the interaction of tectonics and deep mantle flow. *Nature 2016 533:7602*, **533**, 239–242, Nature Publishing Group. doi:10.1038/nature17422

Heyn, B.H., Conrad, C.P. & Trønnes, R.G. (2018) Stabilizing Effect of Compositional Viscosity Contrasts on Thermochemical Piles. *Geophys Res Lett*. doi:10.1029/2018GL078799

Houseman, G.A. & Molnar, P. (1997) Gravitational (Rayleigh-Taylor) instability of a layer with non-linear viscosity and convective thinning of continental lithosphere. *Geophys J Int*, **128**, 125–150, John Wiley & Sons, Ltd. doi:10.1111/J.1365-246X.1997.TB04075.X

Ida, S., Nakagawa, Y. & Nakazawa, K. (1987) The Earth's core formation due to the Rayleigh-Taylor instability. *Icarus*, **69**, 239–248, Academic Press. doi:10.1016/0019-1035(87)90103-5

Jellinek, A.M., Lenardic, A. & Manga, M. (2002) The influence of interior mantle temperature on the structure of plumes: Heads for Venus, Tails for the Earth. *Geophys Res Lett*, **29**, 27–1, John Wiley & Sons, Ltd. doi:10.1029/2001GL014624

Jellinek, A.M. & Manga, M. (2004) LINKS BETWEEN LONG-LIVED HOT SPOTS, MANTLE PLUMES, D″, AND PLATE TECTONICS. *Reviews of Geophysics*, **42**, John Wiley & Sons, Ltd. doi:10.1029/2003RG000144

Jones, T.D., Davies, D.R., Campbell, I.H., Wilson, C.R. & Kramer, S.C. (2016) Do mantle plumes preserve the heterogeneous structure of their deep-mantle source? *Earth Planet Sci Lett*, **434**, 10–17, Elsevier B.V. doi:10.1016/j.epsl.2015.11.016

Keken, P.E. van, King, S.D., Schmeling, H., Christensen, U.R., Neumeister, D. & Doin, M.-P. (1997) A comparison of methods for the modeling of thermochemical convection. *J Geophys Res Solid Earth*, **102**, 22477–22495, American Geophysical Union (AGU). doi:10.1029/97jb01353

Kerr, R.C., Lister, J.R., Kerr, R.C. & Lister, J.R. (2008) Rise and deflection of mantle plume tails. *Geochemistry, Geophysics, Geosystems*, **9**, 10004, John Wiley & Sons, Ltd. doi:10.1029/2008GC002124

Kerr, R.C. & Mériaux, C. (2004) Structure and dynamics of sheared mantle plumes. *Geochemistry, Geophysics, Geosystems*, **5**. doi:10.1029/2004GC000749

Koppers, A.A.P., Becker, T.W., Jackson, M.G., Konrad, K., Müller, R.D., Romanowicz, B., Steinberger, B., *et al.* (2021) Mantle plumes and their role in Earth processes. *Nature Reviews Earth & Environment 2021 2:6*, **2**, 382–401, Nature Publishing Group. doi:10.1038/s43017-021-00168-6

Korenaga, J. (2005) Firm mantle plumes and the nature of the core-mantle boundary region. *Earth Planet Sci Lett*. doi:10.1016/j.epsl.2005.01.016

Kumagai, I., Davaille, A. & Kurita, K. (2007) On the fate of thermally buoyant mantle plumes at density interfaces. *Earth Planet Sci Lett*, **254**, 180–193, Elsevier. doi:10.1016/J.EPSL.2006.11.029

Lei, W., Ruan, Y., Bozdağ, E., Peter, D., Lefebvre, M., Komatitsch, D., Tromp, J., *et al.* (2020) Global adjoint tomography—model GLAD-M25. *Geophys J Int*, **223**, 1–21, Oxford Academic. doi:10.1093/GJI/GGAA253

Lemiale, V., Mühlhaus, H.B., Moresi, L. & Stafford, J. (2008) Shear banding analysis of plastic models formulated for incompressible viscous flows. *Physics of the Earth and Planetary Interiors*, **171**, 177–186. doi:10.1016/j.pepi.2008.07.038

Li, M. & Zhong, S. (2017) The source location of mantle plumes from 3D spherical models of mantle convection. *Earth Planet Sci Lett*, **478**, 47–57, Elsevier. doi:10.1016/J.EPSL.2017.08.033

Mansour, J., Giordani, J., Moresi, L., Beucher, R., Kaluza, O., Velic, M., Farrington, R., *et al.* (2020) Underworld2: Python Geodynamics Modelling for Desktop, HPC and Cloud. *J Open Source Softw*, **5**, 1797, The Open Journal. doi:10.21105/joss.01797

Masse, L. (2007) Stabilizing effect of anisotropic thermal diffusion on the ablative Rayleigh-Taylor instability. *Phys Rev Lett*, **98**, 245001, American Physical Society. doi:10.1103/PHYSREVLETT.98.245001/FIGURES/5/MEDIUM

McNamara, A.K. & Zhong, S. (2004) Thermochemical structures within a spherical mantle: Superplumes or piles? *J Geophys Res Solid Earth*, **109**, 7402, John Wiley & Sons, Ltd. doi:10.1029/2003JB002847

Meer, D.G. van der, Hinsbergen, D.J.J. van & Spakman, W. (2018) Atlas of the underworld: Slab remnants in the mantle, their sinking history, and a new outlook on lower mantle viscosity. *Tectonophysics*, **723**, 309–448, Elsevier. doi:10.1016/J.TECTO.2017.10.004

Mikaelian, K.O. (1996) Rayleigh-Taylor instability in finite-thickness fluids with viscosity and surface tension. *Phys Rev E*, **54**, 3676, American Physical Society. doi:10.1103/PhysRevE.54.3676

Miller, N.C. & Behn, M.D. (2012) Timescales for the growth of sediment diapirs in subduction zones. *Geophys J Int*, **190**, 1361–1377, John Wiley & Sons, Ltd. doi:10.1111/J.1365-246X.2012.05565.X

Mondal, P. & Korenaga, J. (2018) The Rayleigh–Taylor instability in a self-gravitating two-layer viscous sphere. *Geophys J Int*, **212**, 1859–1867, Oxford Academic. doi:10.1093/GJI/GGX507

Montague, N.L. & Kellogg, L.H. (2000) Numerical models of a dense layer at the base of the mantle and implications for the geodynamics of D″. *J Geophys Res Solid Earth*, **105**, 11101–11114, Blackwell Publishing Ltd. doi:10.1029/1999JB900450

Moresi, L., Quenette, S., Lemiale, V., Mériaux, C., Appelbe, B. & Mühlhaus, H.B. (2007) Computational approaches to studying non-linear dynamics of the crust and mantle. *Physics of the Earth and Planetary Interiors*. doi:10.1016/j.pepi.2007.06.009

Morgan, W. J. (1971) Convection Plumes in the Lower Mantle. *Nature 1971 230:5288*, **230**, 42–43, Nature Publishing Group. doi:10.1038/230042a0

Morgan, W. Jason. (1972) Deep Mantle Convection Plumes and Plate Motions. *Am Assoc Pet Geol Bull*, **56**, 203–213, American Association of Petroleum Geologists. Retrieved from http://archives.datapages.com/data/bulletns/1971-73/data/pg/0056/0002/0200/0203.htm

Munro, D.H. (1988) Analytic solutions for Rayleigh-Taylor growth rates in smooth density gradients. *Phys Rev A (Coll Park)*, **38**, 1433, American Physical Society. doi:10.1103/PhysRevA.38.1433

Nakada, M., Iriguchi, C. & Karato, S. ichiro. (2012) The viscosity structure of the D″ layer of the Earth's mantle inferred from the analysis of Chandler wobble and tidal deformation. *Physics of the Earth and Planetary Interiors*, **208–209**, 11–24, Elsevier. doi:10.1016/J.PEPI.2012.07.002

Neil, E.A. & Houseman, G.A. (1999) Rayleigh–Taylor instability of the upper mantle and its role in intraplate orogeny. *Geophys J Int*, **138**, 89–107, Oxford Academic. doi:10.1046/J.1365-246X.1999.00841.X

Nipin, L. & Tomar, G. (2015) Effect of viscosity contrast on plume formation in density stratified fluids. *Chem. Eng. Sci.*, **134**, 510–520. doi:10.1016/j.ces.2015.05.044

Nolet, G., Allen, R. & Zhao, D. (2007) Mantle plume tomography. *Chem Geol*, **241**, 248–263, Elsevier. doi:10.1016/J.CHEMGEO.2007.01.022

Olson, P., Silver, P.G. & Carlson, R.W. (1990) The large-scale structure of convection in the Earth's mantle. *Nature 1990 344:6263*, **344**, 209–215, Nature Publishing Group. doi:10.1038/344209a0

Pullin, D.I. (1982) Numerical studies of surface-tension effects in nonlinear Kelvin–Helmholtz and Rayleigh–Taylor instability. *J Fluid Mech*, **119**, 507–532, Cambridge University Press. doi:10.1017/S0022112082001463

Ramberg, H. (1968) Instability of layered systems in the field of gravity. I. *Physics of the Earth and Planetary Interiors*, **1**, 427–447, Elsevier. doi:10.1016/0031-9201(68)90014-9

Ramberg, H. (1968) Instability of layered systems in the field of gravity. II. *Physics of the Earth and Planetary Interiors*, **1**, 448–474, Elsevier. doi:10.1016/0031-9201(68)90015-0

Ramberg, H. (1972) Theoretical models of density stratification and diapirism in the Earth. *J Geophys Res*, **77**, 877–889, John Wiley & Sons, Ltd. doi:10.1029/JB077I005P00877

Rayleigh. (1882) Investigation of the Character of the Equilibrium of an Incompressible Heavy Fluid of Variable Density. *Proceedings of the London Mathematical Society*, **s1-14**, 170–177, Oxford Academic. doi:10.1112/PLMS/S1-14.1.170

Richards, M. A. & Hager, B.H. (1984) Geoid anomalies in a dynamic earth. *J. geophys. Res.*, **89**, 5987–6002. doi:10.1029/jb089ib07p05987

Richards, Mark A. & Griffiths, R.W. (1989) Thermal entrainment by deflected mantle plumes. *Nature 1989 342:6252*, **342**, 900–902, Nature Publishing Group. doi:10.1038/342900a0

Song, Y., Wang, P. & Wang, L. (2021) Numerical investigations of Rayleigh–Taylor instability with a density gradient layer. *Comput Fluids*, **220**, 104869, Pergamon. doi:10.1016/J.COMPFLUID.2021.104869

Spada, G., Yuen, D.A., Sabadini, R. & Boschi, E. (1991) Lower-mantle viscosity constrained by seismicity around deglaciated regions. *Nature 1991 351:6321*, **351**, 53–55, Nature Publishing Group. doi:10.1038/351053a0

Steinberger, B. & O'Connell, R.J. (1998) Advection of plumes in mantle flow: Implications for hotspot motion, mantle viscosity and plume distribution. *Geophys J Int*, **132**, 412–434, Oxford University Press. doi:10.1046/j.1365-246x.1998.00447.x

Styles, E., Goes, S., Keken, P.E. van, Ritsema, J. & Smith, H. (2011) Synthetic images of dynamically predicted plumes and comparison with a global tomographic model. *Earth Planet Sci Lett*, **311**, 351–363, Elsevier. doi:10.1016/J.EPSL.2011.09.012

Taylor, G. (1950) The instability of liquid surfaces when accelerated in a direction perpendicular to their planes. I. *Proc R Soc Lond A Math Phys Sci*, **201**, 192–196, The Royal Society. doi:10.1098/RSPA.1950.0052

Turcotte, D. & Schubert, G. (2002) *Geodynamics*. Retrieved from https://books.google.com/books?hl=en&lr=&id=-nCHlVuJ4FoC&oi=fnd&pg=PR11&ots=LqWMDVA6YQ&sig=agZlPRf7u0rI9Ryio3A0xOiQo-M

Whitehead, J.A. (1986) Buoyancy-driven instabilities of low-viscosity zones as models of magma-rich zones. *J Geophys Res Solid Earth*, **91**, 9303–9314, John Wiley & Sons, Ltd. doi:10.1029/JB091IB09P09303

Wilcock, W.S.D. & Whitehead, J.A. (1991) The Rayleigh-Taylor instability of an embedded layer of low-viscosity fluid. *J Geophys Res Solid Earth*, **96**, 12193–12200, John Wiley & Sons, Ltd. doi:10.1029/91JB00339

Zrnić, D.S. & Hendricks, C.D. (2003) Stabilization of the Rayleigh-Taylor Instability with Magnetic Feedback. *Phys Fluids*, **13**, 618, American Institute of PhysicsAIP. doi:10.1063/1.1692967.

Figure 1:

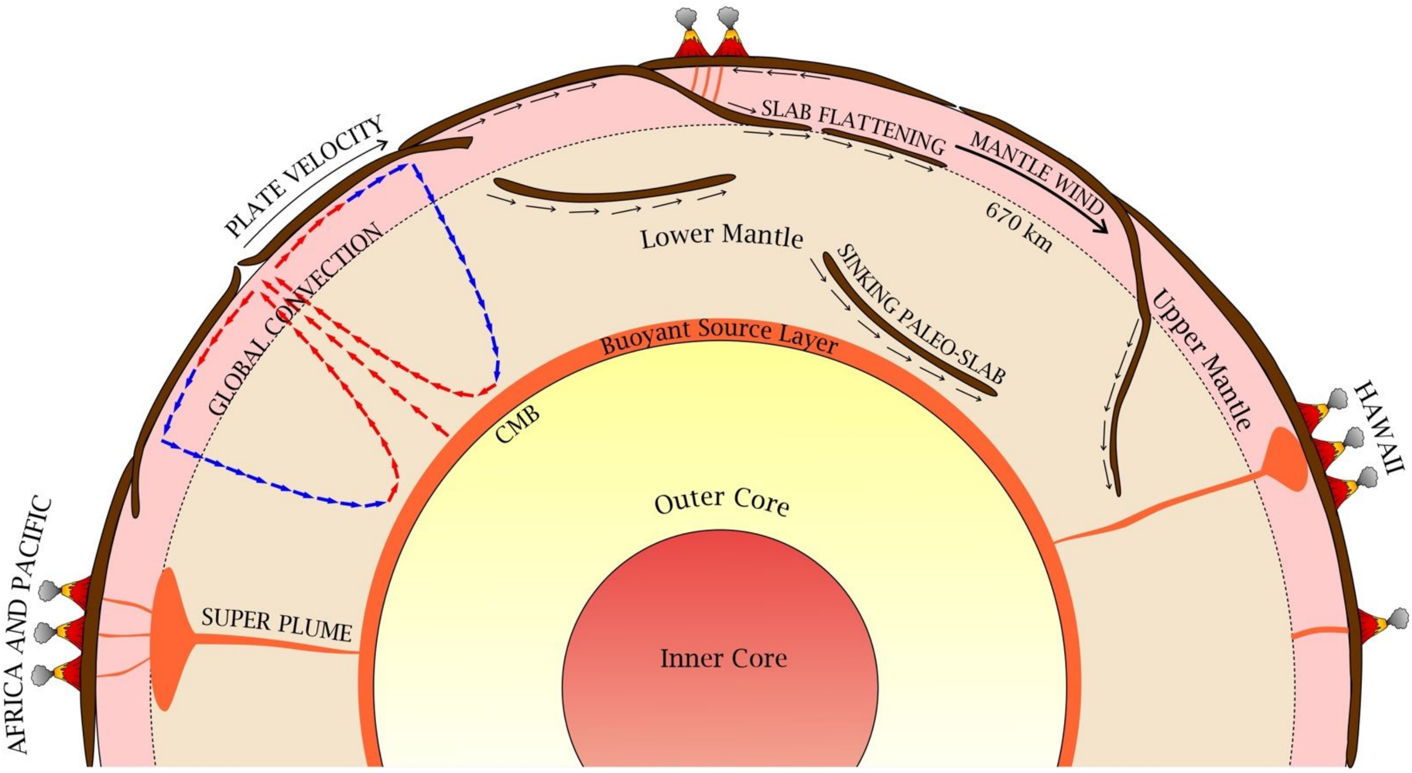

Figure 1: Schematic presentation of the Earth's interior showing major locations of plume generation in the mantle and associated volcanisms on the surface. Different types of mantle flows, such as convection-, sinking slab-, lithospheric plate-driven flows and mantle wind are also depicted. All deep-source plumes, forming hotspots, like the Hawaiian chain, originate from the thermal boundary layer (TBL) at the core-mantle boundary (CMB).

Figure 2:

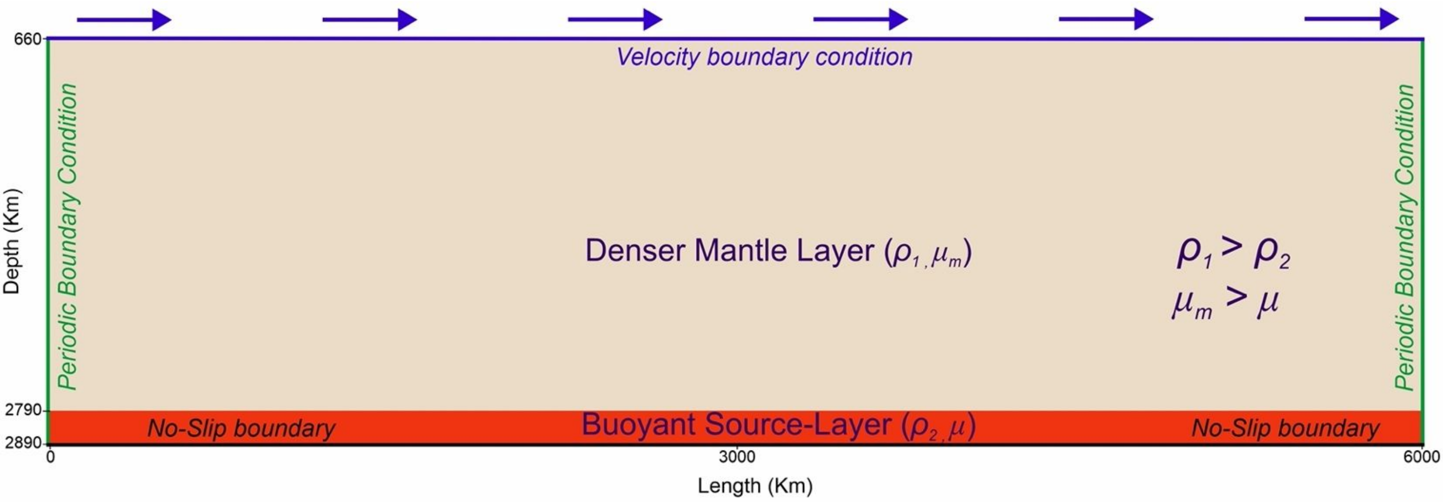

Figure 2: Consideration of the initial CFD model set-up and associated boundary conditions used for simulations of Rayleigh-Taylor instabilities in the lower mantle domain. Denser mantle (ρ_1) overlies a 100 km thick lighter (ρ_2) layer (source layer) at the model base. The model domain is discretized into elements with a mesh resolution of 1024 x 512. The side and the bottom walls are assigned periodic and no-slip boundary conditions, respectively. The top model boundary is imposed with a uniform horizontal velocity, which induces an initial global horizontal flow condition in the overlying denser mantle.

Figure 3:

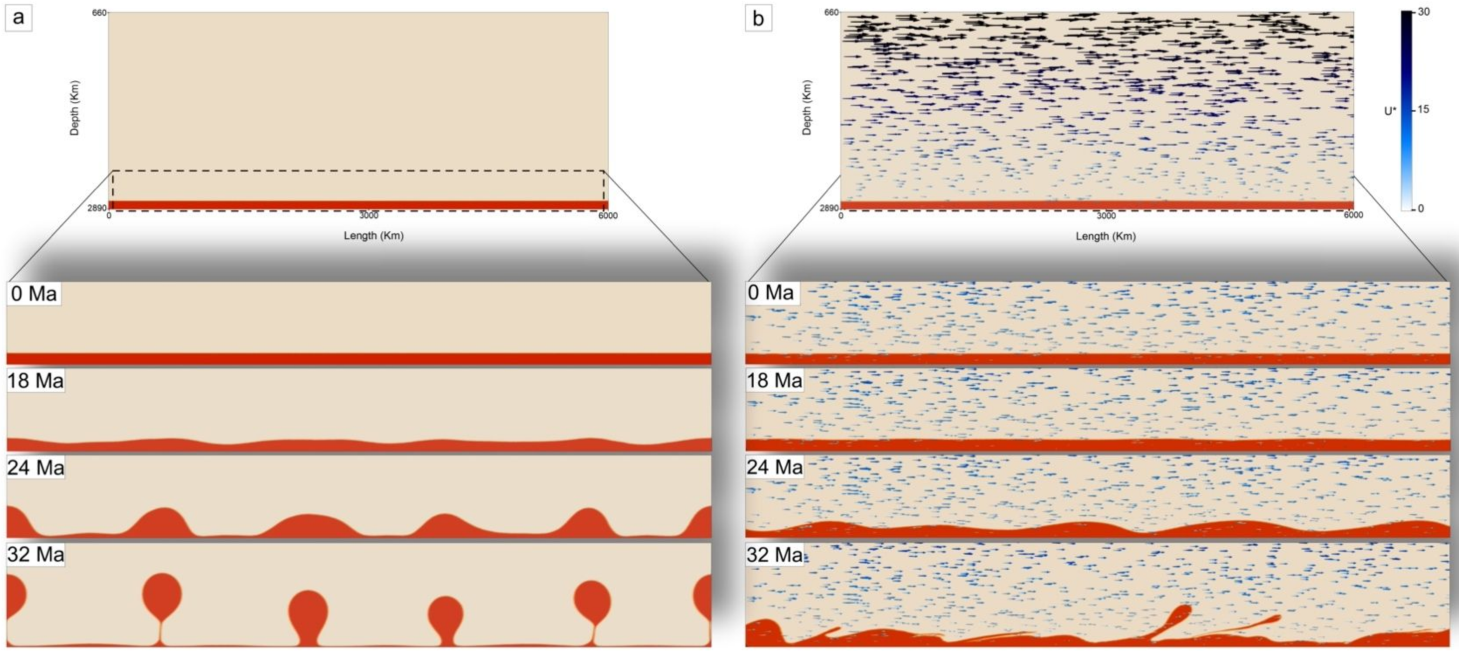

Figure 3: Progressive growth of Rayleigh-Taylor instabilities in CFD model simulations. a) Reference experiment with an initially rest mantle condition (U^{*}= 0). b) Experiment with an initial horizontal global flow (U^{*}=30) in the mantle. Notice in panel (b) at t = 32 Ma that the instability growth is significantly dampened by the global mantle flow. The colour bar represents normalized flow velocity magnitudes.

Figure 4:

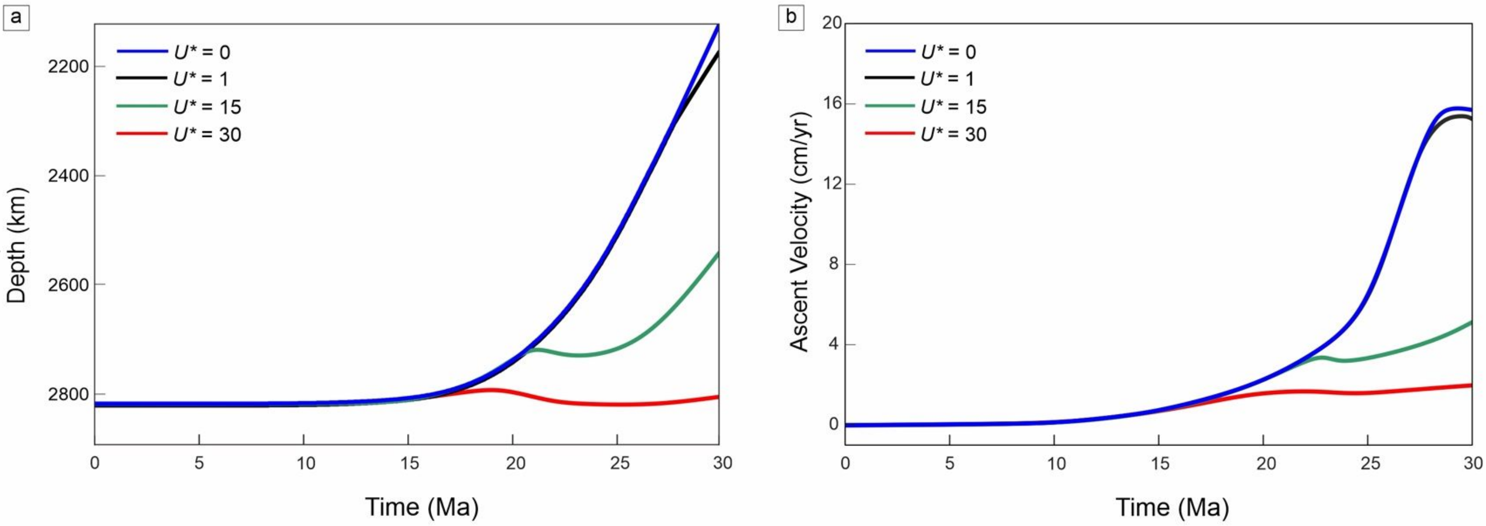

Figure 4: Graphical plots of a) plume ascent heights, and b) vertical ascent velocities of the fastest growing instabilities as a function of time for different normalized global flow-velocity magnitudes (U^*). Note that increasing U^* strongly influences the ascent heights and velocities at $t > 18$ Ma.

Figure 5:

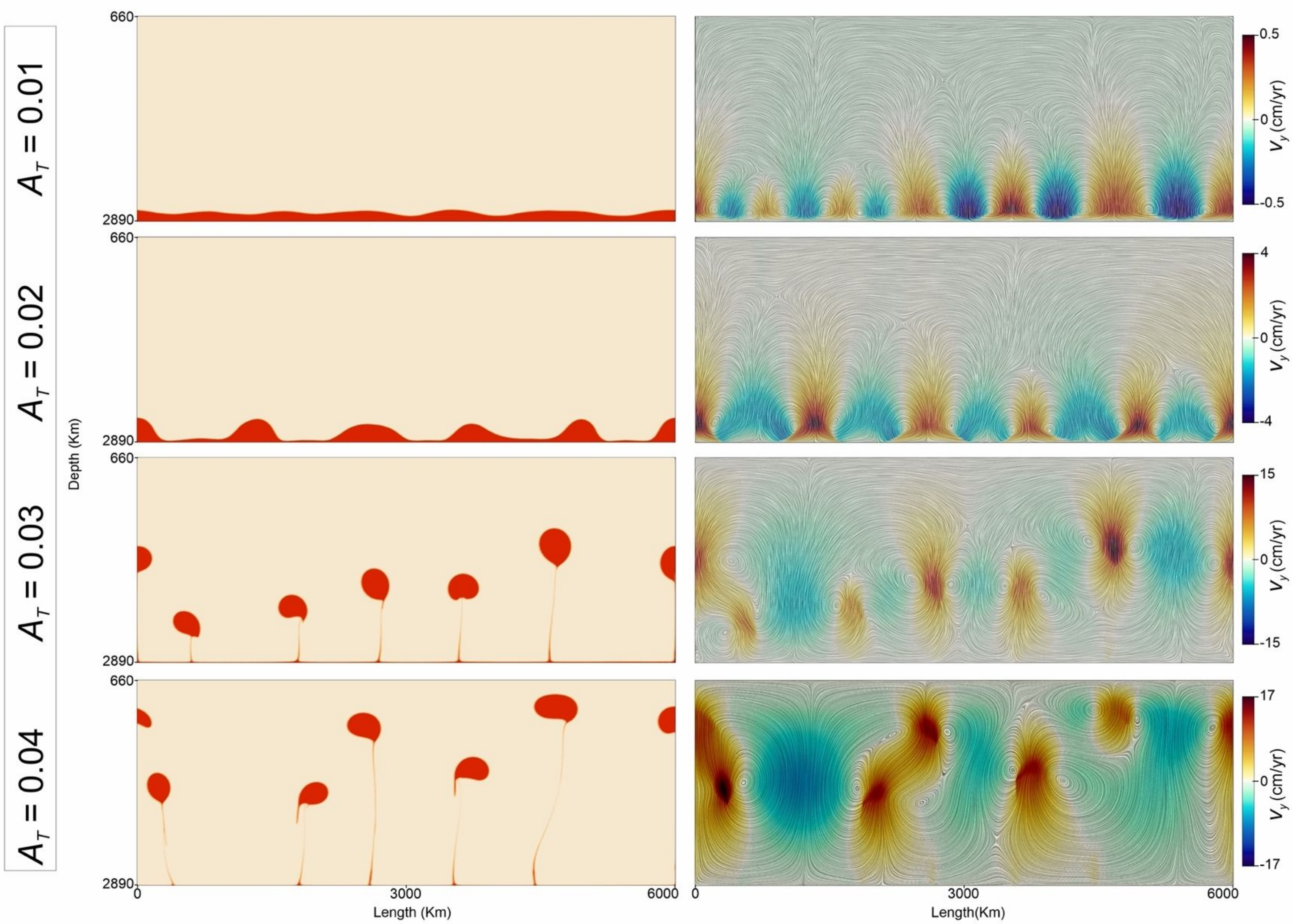

Figure 5: CFD simulations showing the effects of buoyancy factor (A_T) on a) Rayleigh-Taylor instability growth in the buoyant source layers (red colour) and b) the corresponding flow fields represented by streamlines. The colour contours depict the magnitudes of vertical velocity components. The snapshots of four different simulations presented in the row-wise panels correspond to a simulation time of 22 Ma.

Figure 6:

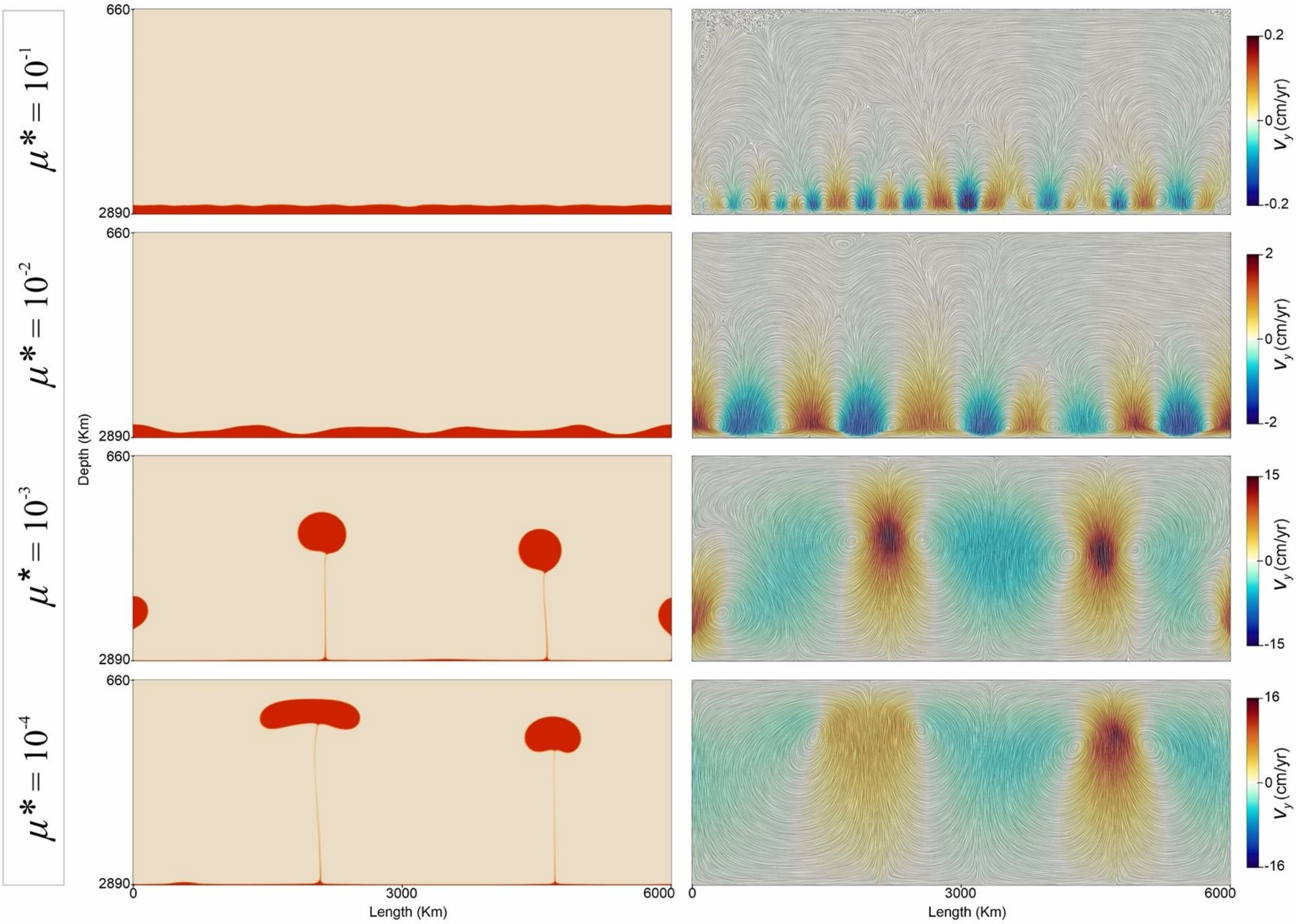

Figure 6: Effects of the normalized source-layer viscosity (μ^*) on a) Rayleigh-Taylor instability growth and b) the corresponding flow fields in CFD models. The colour contours depict the magnitudes of vertical velocity components. The snapshots of four different simulations presented in the row-wise panels correspond to a simulation time of 20 Ma.

Figure 7:

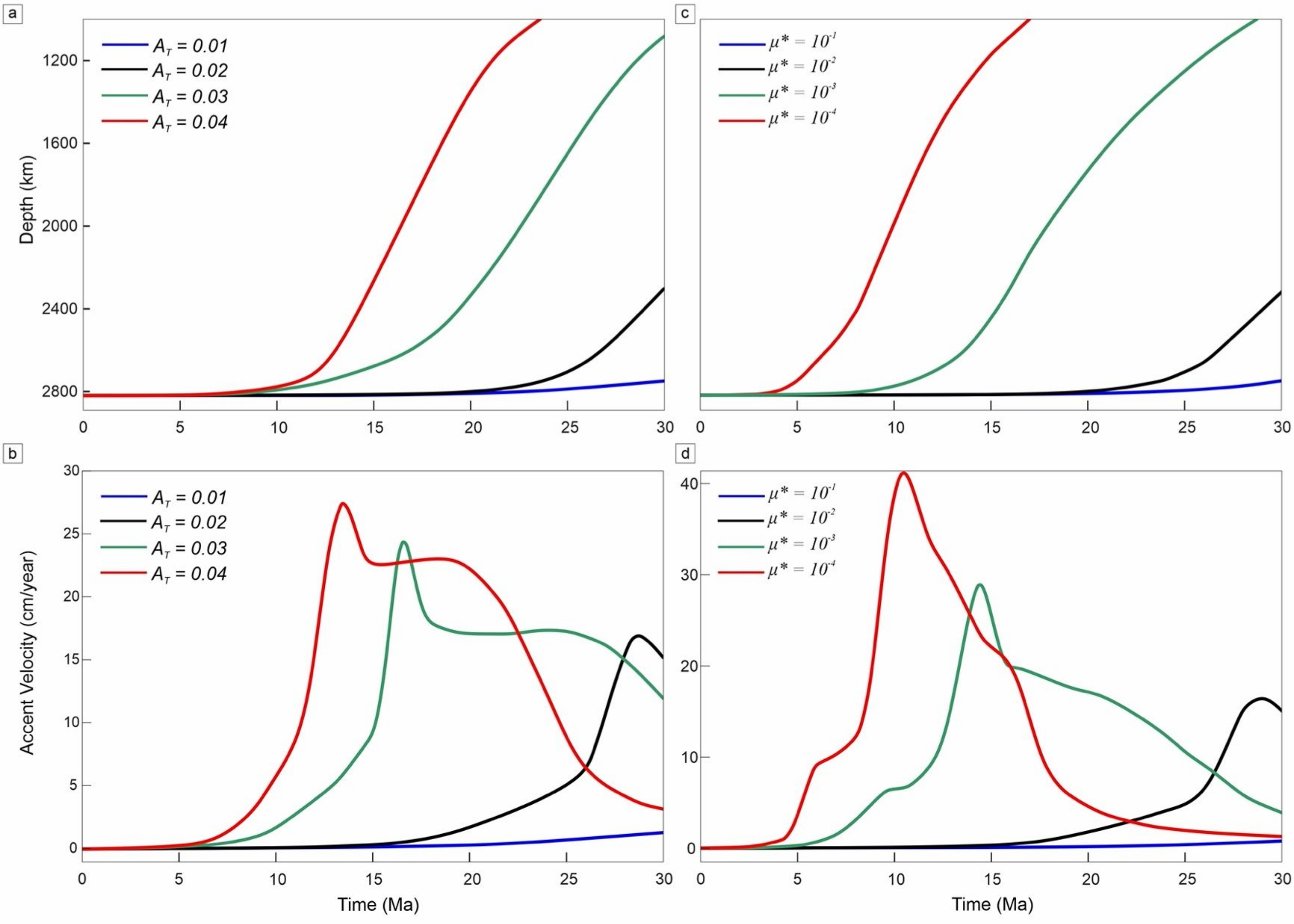

Figure 7: Time series analyses of the plume ascent heights and the vertical ascent velocities of the fastest growing instabilities for different A_T values in a) and b), and μ^* values in c) and d), respectively.

Figure 8:

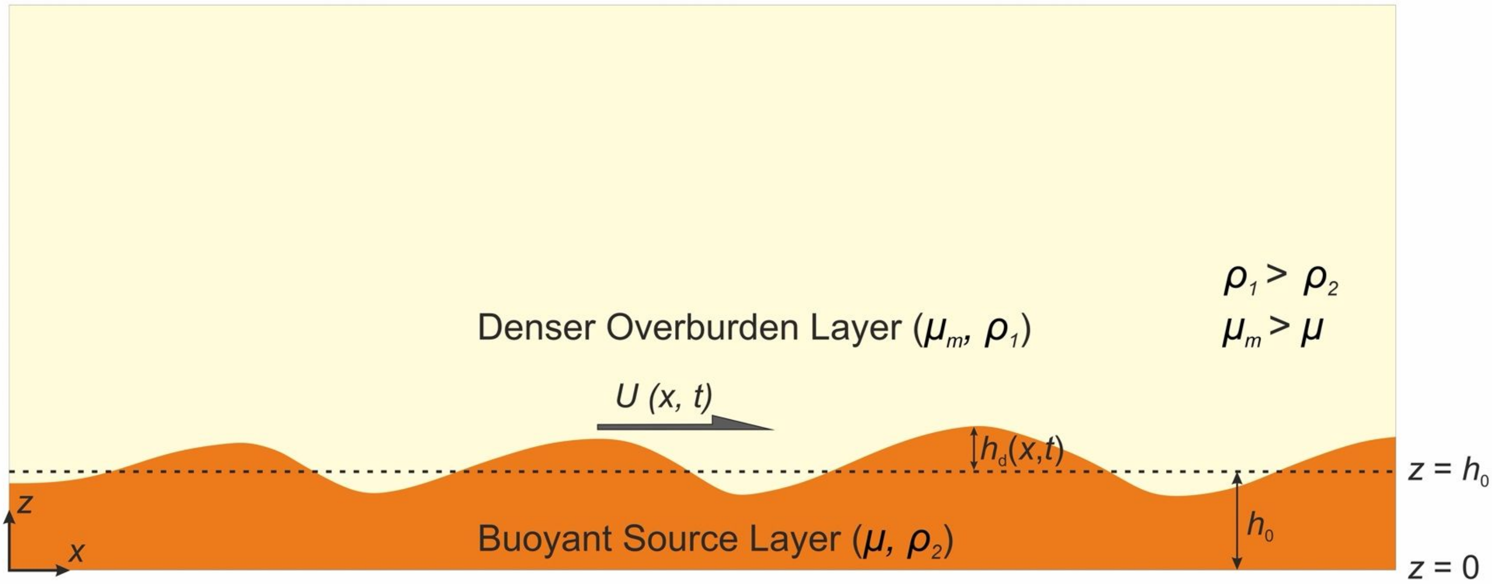

Figure 8: Theoretical consideration for the linear stability analysis: a thin buoyant layer (source layer) (density: ρ_2 and viscosity: μ) underlying a denser fluid layer (density: ρ_1 and viscosity: μ_M) (ambient mantle). Dashed and solid lines denote the initial source-layer configuration and the deformed interface geometry formed by RTI. h_o and h_d define the initial source-layer thickness and the vertical deflection at the interface, respectively. *U(x,t)* represents the horizontal flow velocity at the interface.

Figure 9:

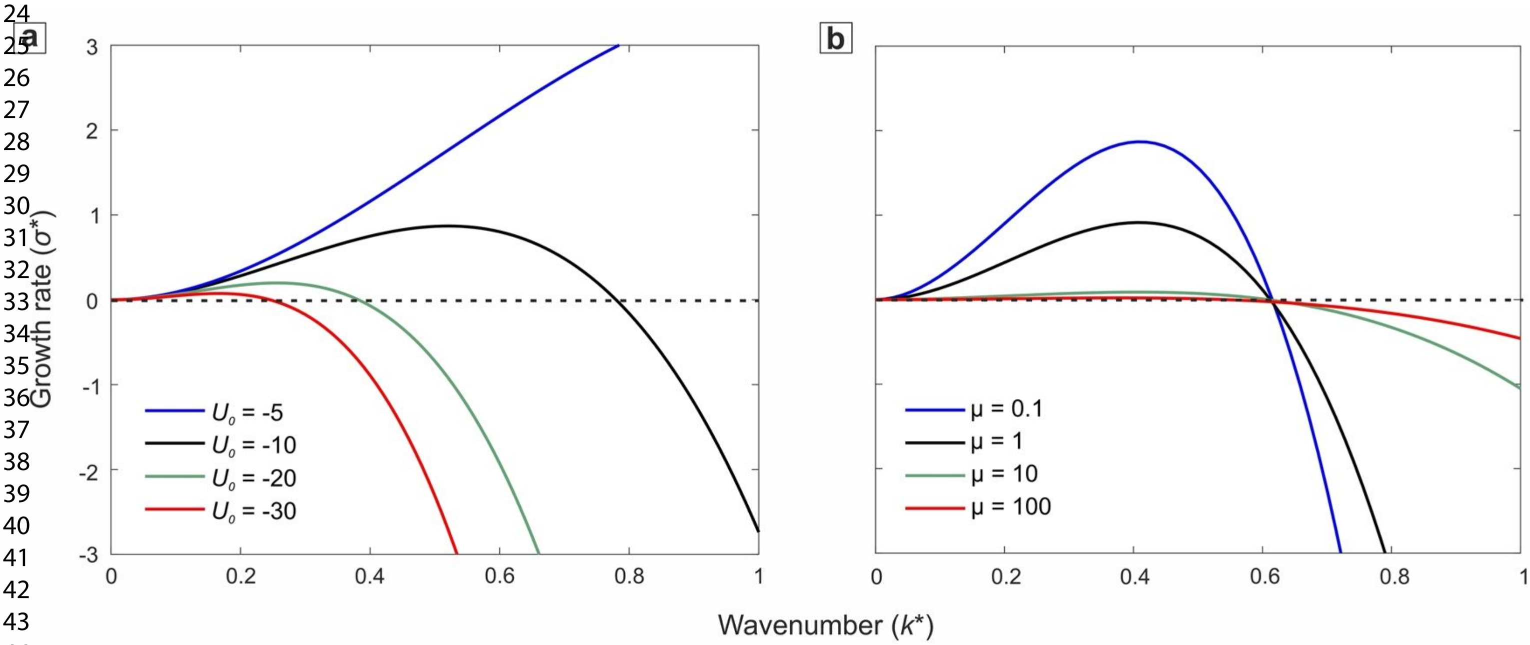

Figure 9: Normalized growth rates (σ^*) versus normalized wavenumber (k^*) plots for different values of (a) ambient mantle velocity (U_0), and (b) source layer viscosity (μ^*) obtained from the linear stability analysis.

Figure 10:

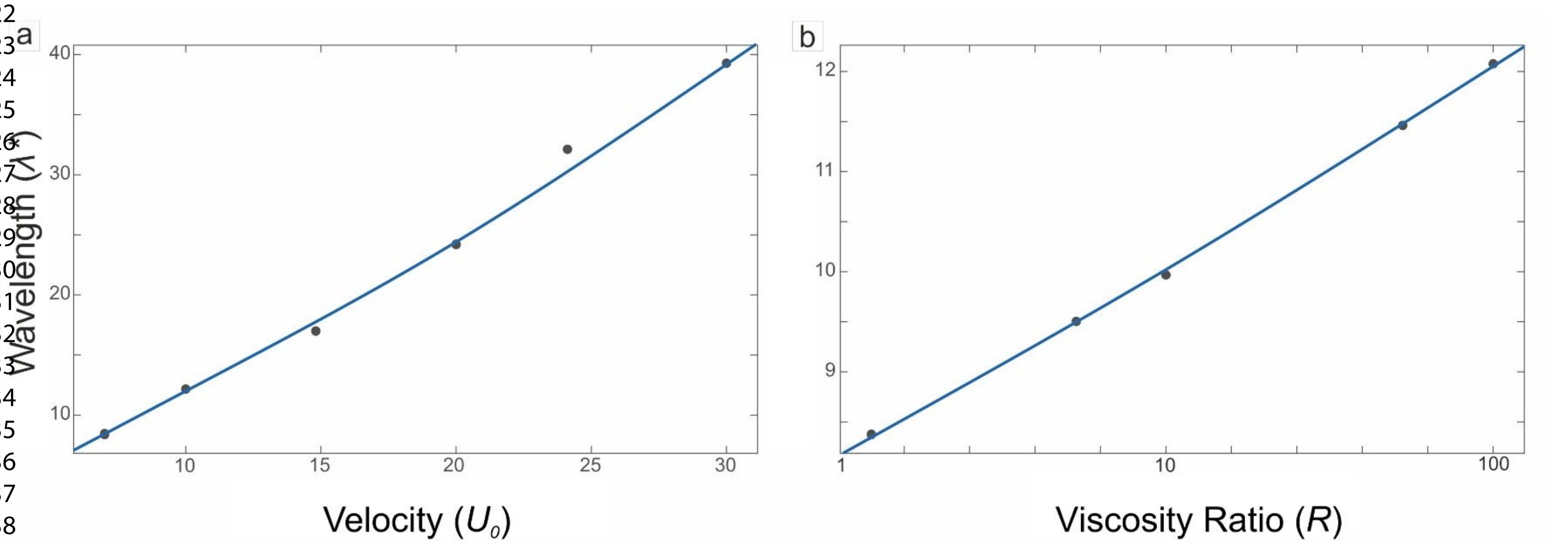

Figure 10: Variations of the instability wavelength (λ^*) with (a) global flow velocity (U_0), and (b) mantle-source layer viscosity ratio ($R = \frac{\mu_M}{\mu}$) from the linear stability analysis. All the variables are presented as non-dimensional quantities.

Figure 11:

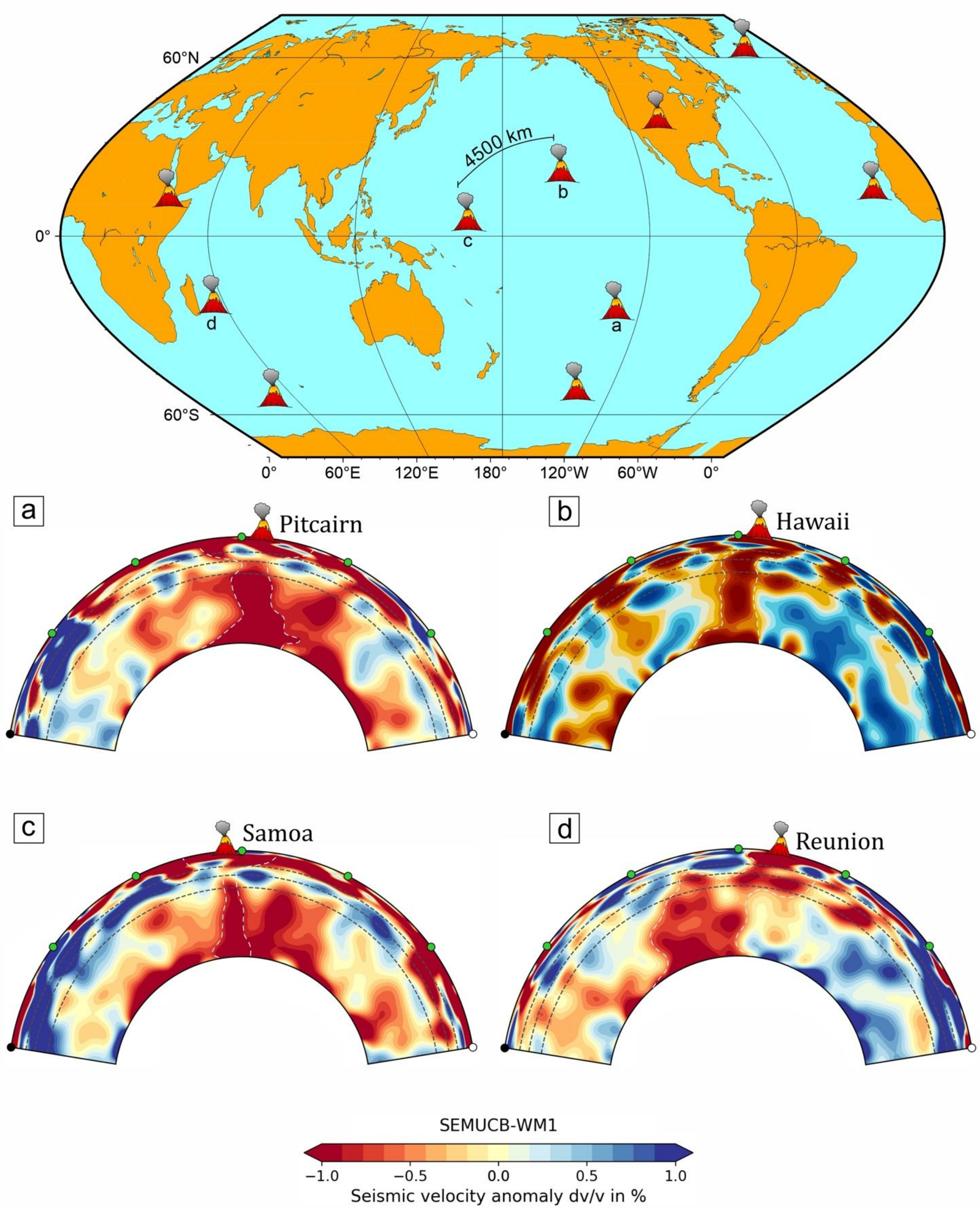
60°N
0°
60°S
4500 km
a
b
c
d
0°
60°E
120°E
180°
120°W
60°W
0°
a
Pitcairn
b
Hawaii
c
Samoa
d
Reunion
SEMUCB-WM1
−1.0
−0.5
0.0
0.5
1.0
Seismic velocity anomaly dv/v in %

Figure 11: Global distribution of the major hotspots originating from deep-mantle plume sources. The seismic sections (lower panels) show the plume configurations in mantle beneath a) Pitcairn, b) Hawaii, c) Samoa, and d) Afar hotspots. Note that inter-hotspot distances are several thousand kilometres.

Supplementary Information for

Dampening effect of global flows on Rayleigh-Taylor instabilities: Implications for deep-mantle plume vis-à-vis hotspot distributions

Arnab Roy, Dip Ghosh and Nibir Mandal

Department of Geological Sciences, Jadavpur University, Kolkata 700032, India

S1. Analytical solution for plume growth velocity:

This is a typical analytical solution for velocity of plume growth (v_y) first shown by Ramberg (1968). Let an initial sinusoidal disturbance at the boundary between the two layers (upper (η_1, ρ_1) and lower (η_2, ρ_2)) of thicknesses h_1 and h_2, respectively, have a small initial amplitude (ΔA) and a wavelength (λ). Let $\rho_1 > \rho_2$ and $\eta_1 > \eta_2$ and g is the acceleration due to gravity. The bottom boundary is considered no-slip whereas the side walls are assumed to be in periodic condition. Under this condition, the velocity of the diapiric growth (v_y) is given by the relation (Ramberg, 1968):

$$\frac{v_y}{\Delta A} = -K\,\frac{\rho_1 - \rho_2}{2\eta_2} h_2 g\ ,$$

where the non-dimensional growth factor $(K) = -\frac{a_{12}}{b_{11}j_{22} - a_{12}i_{21}}$, and

$$\omega_1 = \frac{2\pi h_1}{\lambda}\ , \qquad \omega_2 = \frac{2\pi h_2}{\lambda},$$

$$b_{11} = \frac{\eta_1 2{\omega_1}^2}{\eta_2\ (cosh\,2\omega_1 - 1 - 2{\omega_1}^2)} - \frac{2{\omega_2}^2}{cosh\,2\omega_2 - 1 - 2{\omega_2}^2},$$

$$a_{12} = \frac{\eta_1(\sinh 2\omega_1 - 2\omega_1)}{\eta_2\ (cosh\,2\omega_1 - 1 - 2{\omega_1}^2)} - \frac{\sinh 2\omega_2 - 2\omega_2}{cosh\,2\omega_2 - 1 - 2{\omega_2}^2},$$

$$i_{21} = \frac{\eta_1\omega_2(\sinh 2\omega_1 - 2\omega_1)}{\eta_2\ (cosh\,2\omega_1 - 1 - 2{\omega_1}^2)} + \frac{\omega_2(\sinh 2\omega_2 + 2\omega_2)}{cosh\,2\omega_2 - 1 - 2{\omega_2}^2},$$

$$j_{22} = \frac{\eta_1 2{\omega_1}^2\omega_2}{\eta_2\ (cosh\,2\omega_1 - 1 - 2{\omega_1}^2)} + \frac{2{\omega_2}^3}{cosh\,2\omega_2 - 1 - 2{\omega_2}^2},$$

S2. Experiment with horizontal mantle flow (U^*=15):

We systematically increased the top model-boundary velocity (U_o) to evaluate the effect of global flows on the growth rates of instabilities in the source layer. The non-dimensional boundary velocity, $U^* = U_o / v_y$ was assigned a value of 15, keeping A_T and μ^* constant.

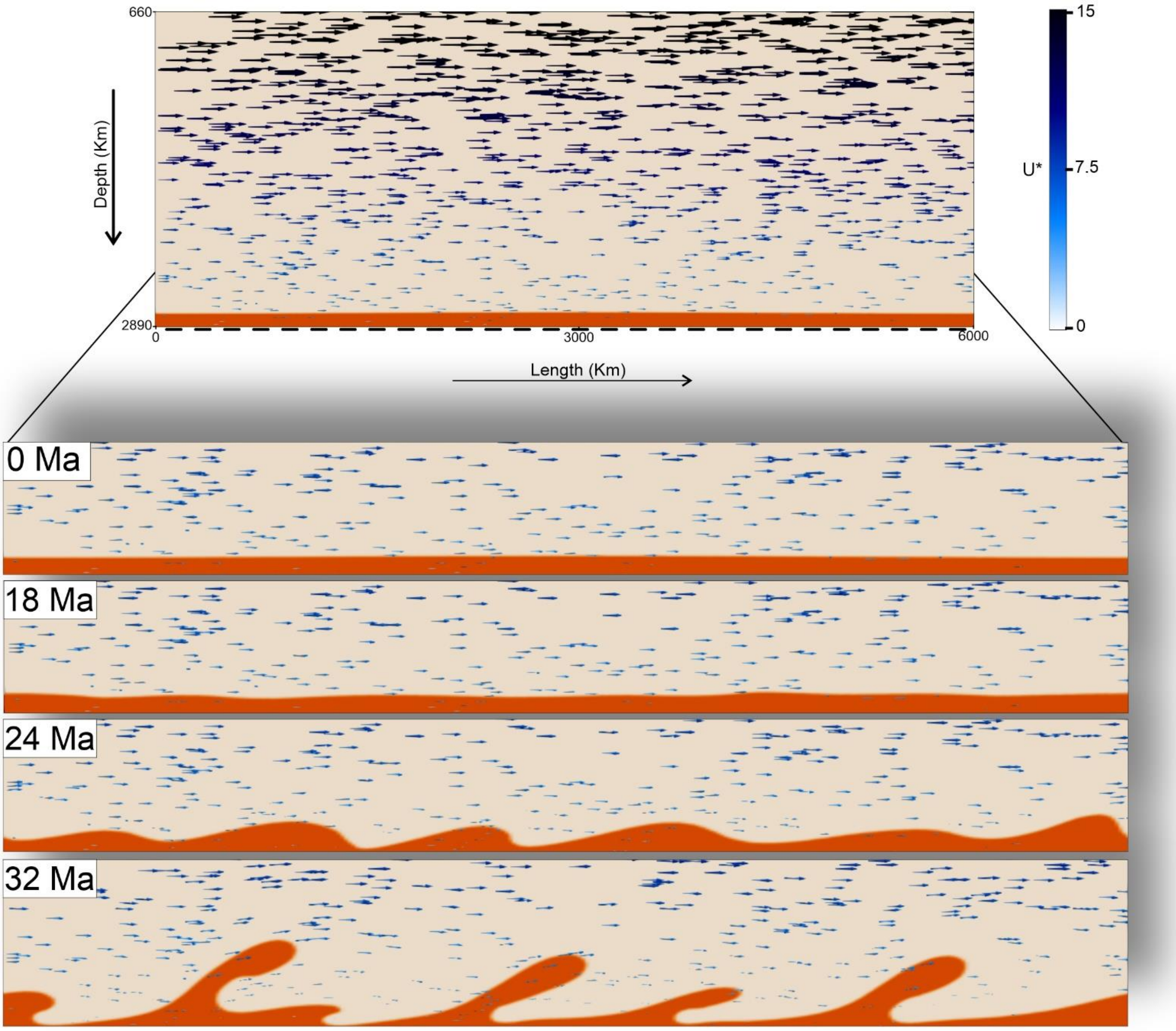

Figure S2: Progressive growth of Rayleigh-Taylor instabilities in CFD model simulations with an initial horizontal global flow (U^*=15) in the mantle.

S3. Experiment with variable Atwood Number (A_T) and source layer viscosity (μ^*):

In this section, we present the detailed progressive growth of Rayleigh-Taylor instabilities in CFD model simulations with A_T = 0.01- 0.04 and μ^*= 10^{-1}- 10^{-4}.

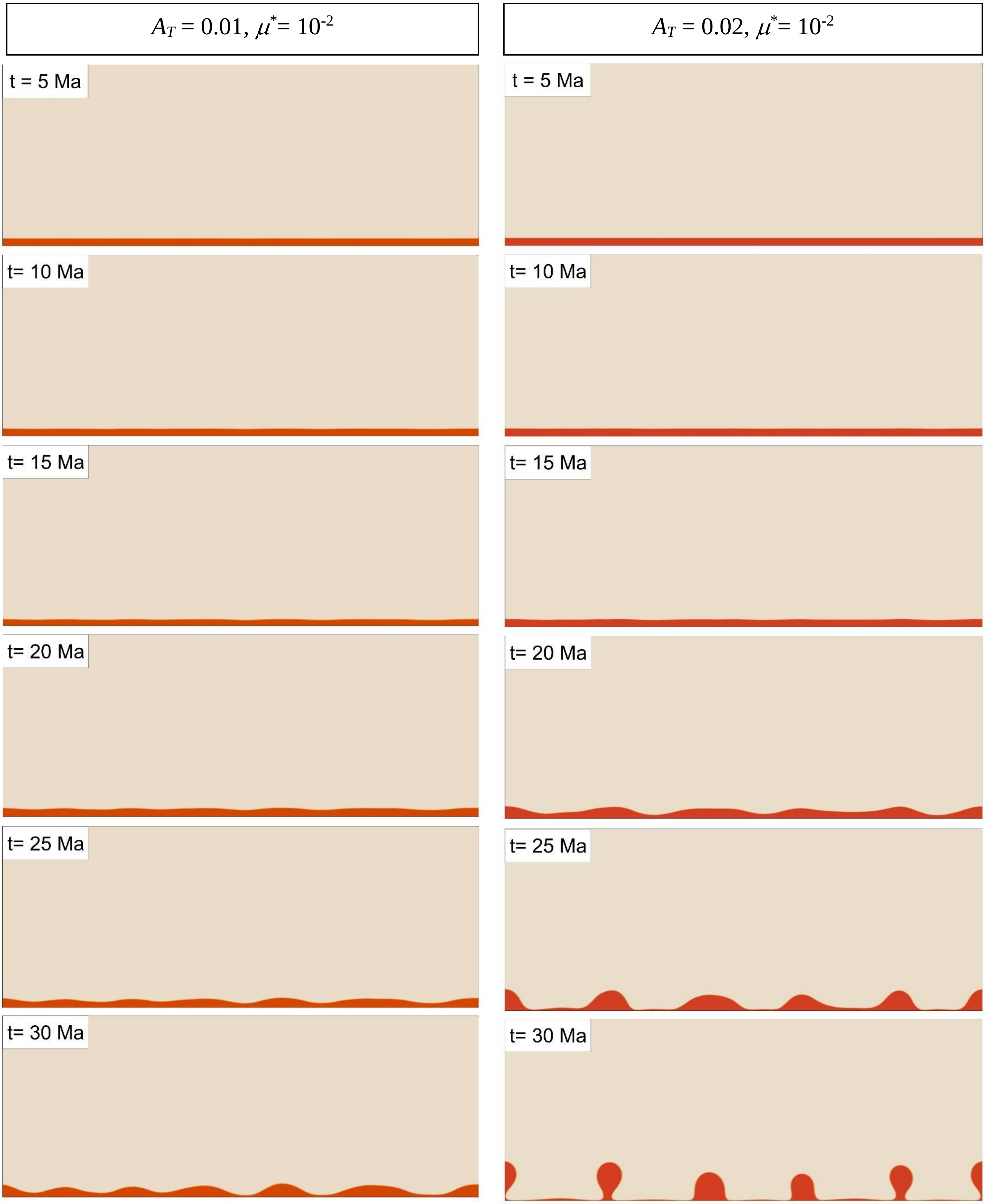

A_T = 0.01, μ^*= 10^{-2}
A_T = 0.02, μ^*= 10^{-2}
t = 5 Ma
t= 10 Ma
t= 15 Ma
t= 20 Ma
t= 25 Ma
t= 30 Ma

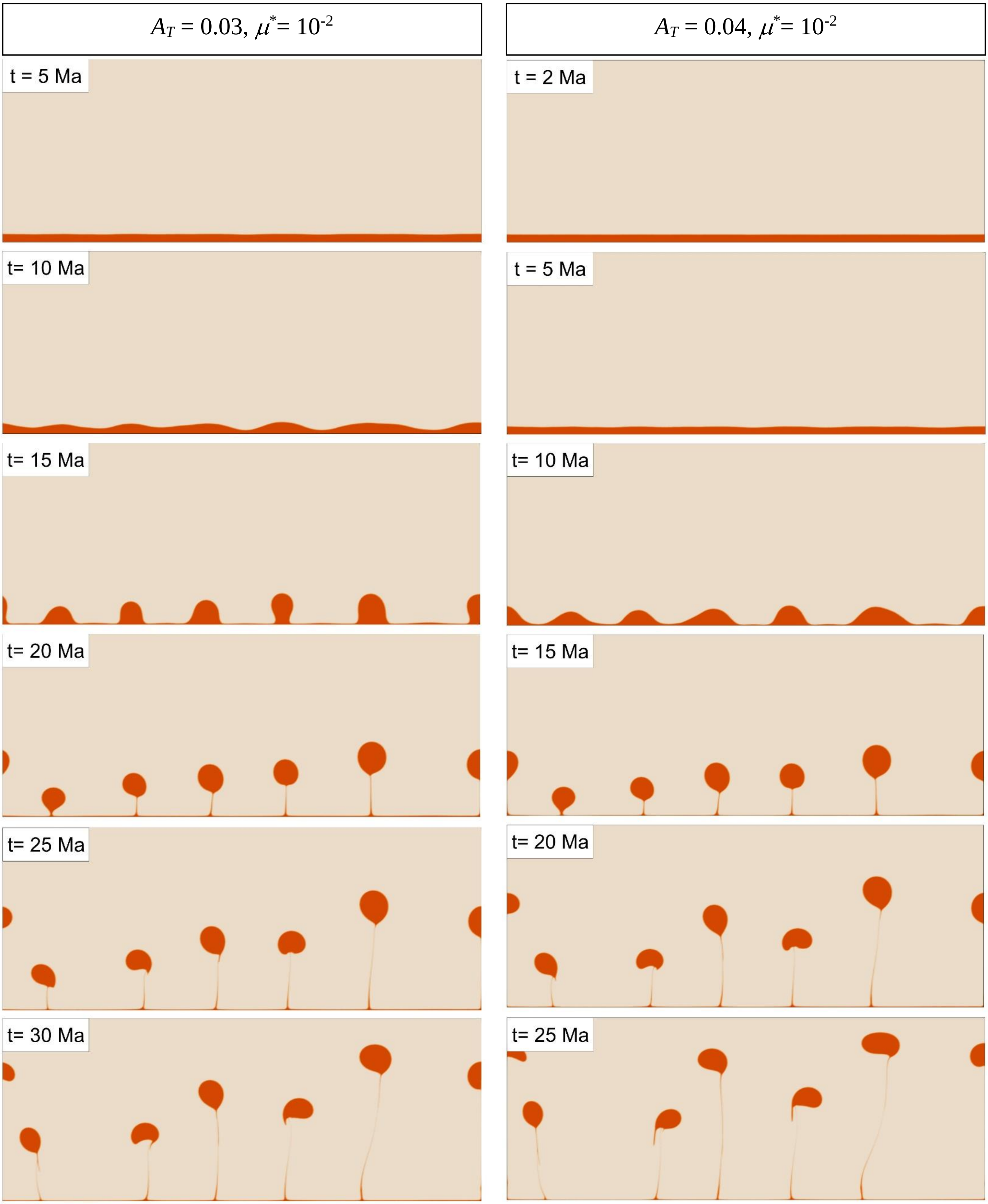

A_T = 0.03, μ^*= 10^{-2}
A_T = 0.04, μ^*= 10^{-2}
t = 5 Ma
t = 2 Ma
t= 10 Ma
t = 5 Ma
t= 15 Ma
t= 10 Ma
t= 20 Ma
t= 15 Ma
t= 25 Ma
t= 20 Ma
t= 30 Ma
t= 25 Ma

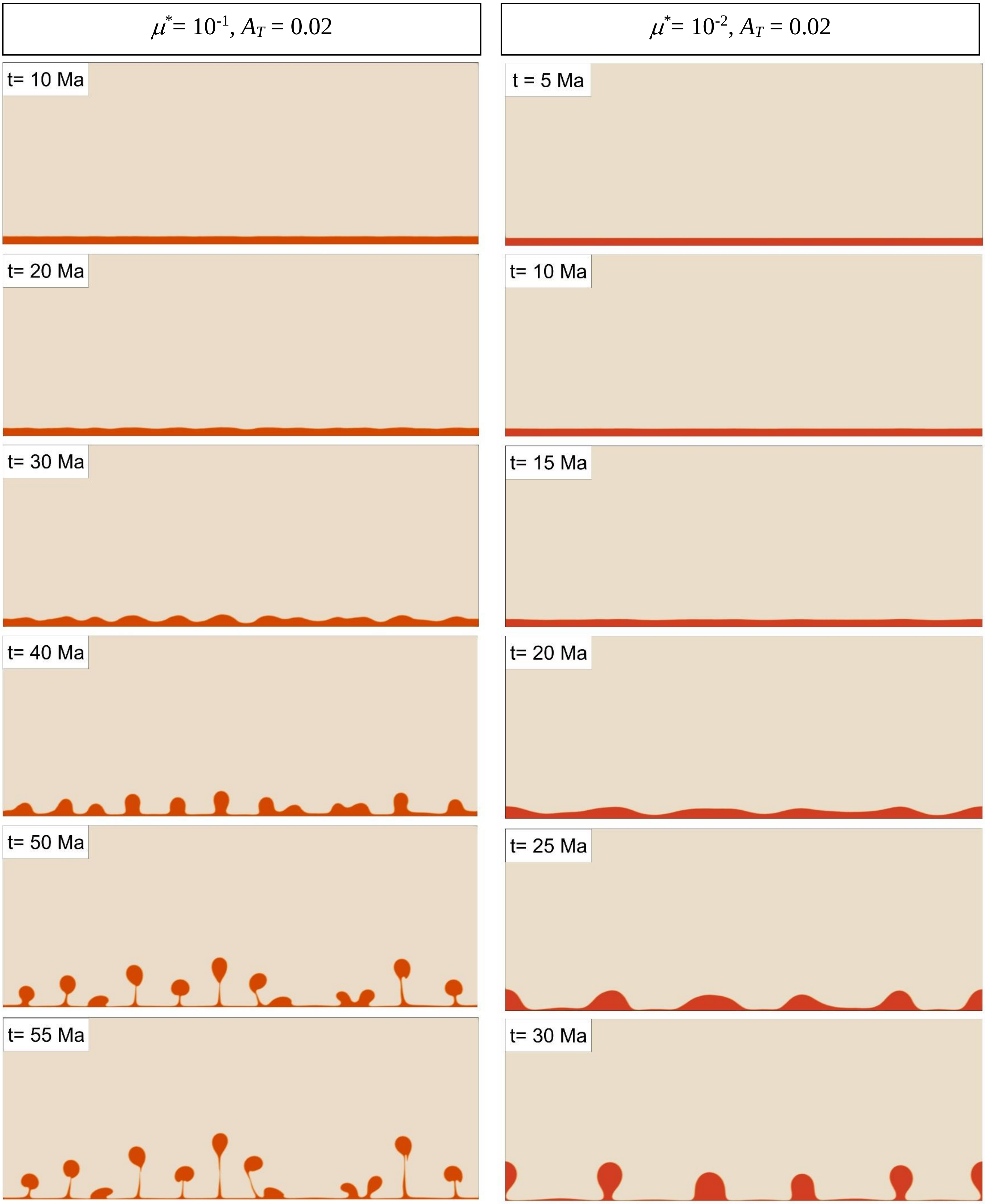
$\mu^* = 10^{-1}$, $A_T = 0.02$
$\mu^* = 10^{-2}$, $A_T = 0.02$
t= 10 Ma
t = 5 Ma
t= 20 Ma
t= 10 Ma
t= 30 Ma
t= 15 Ma
t= 40 Ma
t= 20 Ma
t= 50 Ma
t= 25 Ma
t= 55 Ma
t= 30 Ma

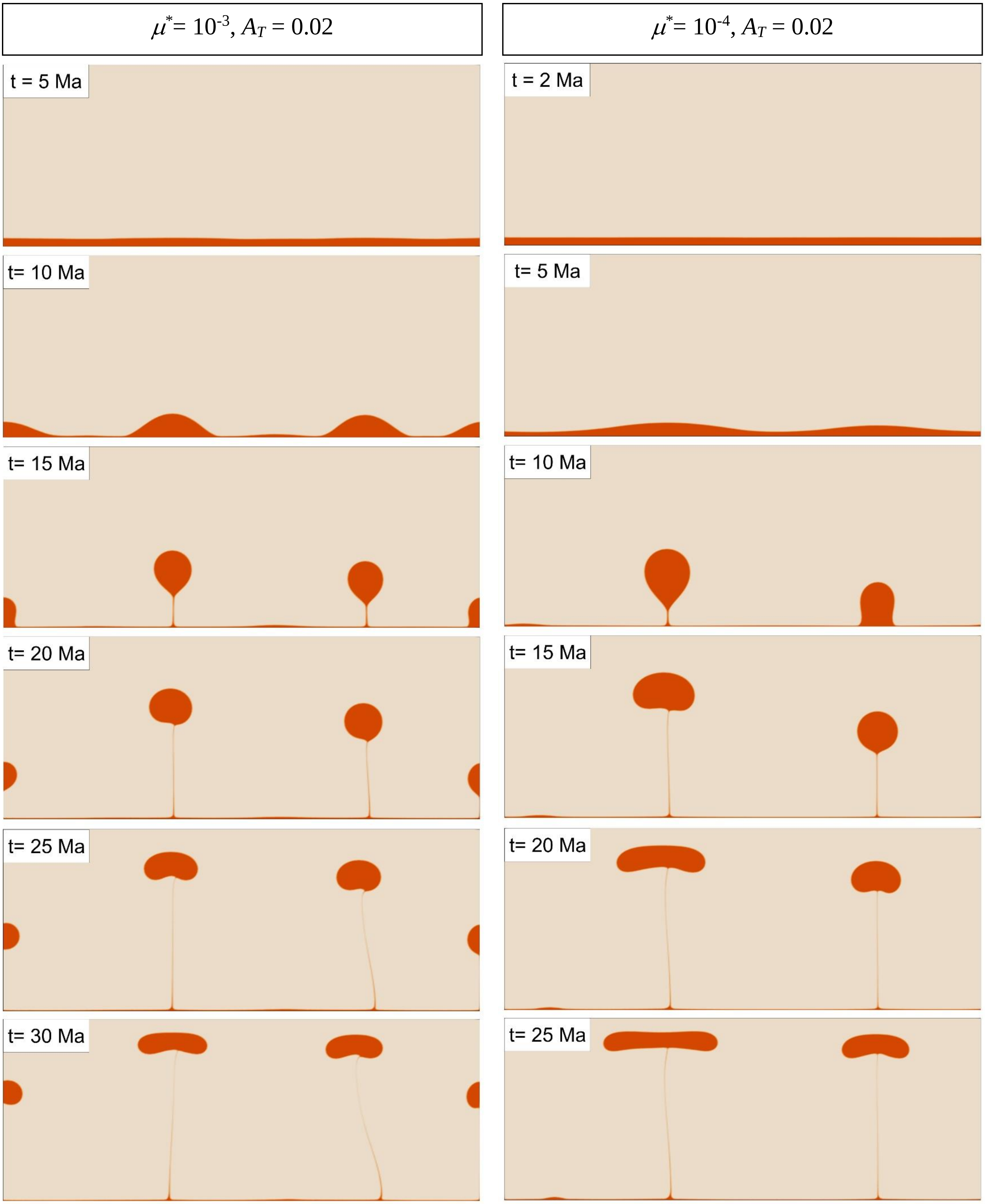

$\mu^* = 10^{-3}$, $A_T = 0.02$
$\mu^* = 10^{-4}$, $A_T = 0.02$
t = 5 Ma
t= 10 Ma
t= 15 Ma
t= 20 Ma
t= 25 Ma
t= 30 Ma
t = 2 Ma
t= 5 Ma
t= 10 Ma
t= 15 Ma
t= 20 Ma
t= 25 Ma

S4: Analytical Results:

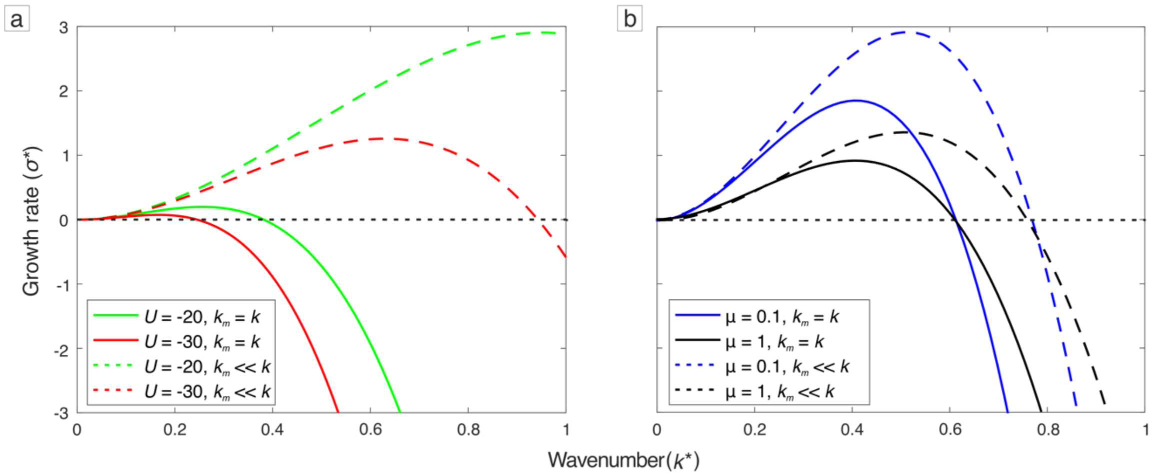

Figure S4: Normalized growth rates (σ^*) versus normalized wavenumber (k^*) plots for different values of (a) ambient mantle velocity (U_0), and (b) source layer viscosity (μ) obtained from the linear stability analysis under the condition of $k_m = k$ and $k_m \ll k$.

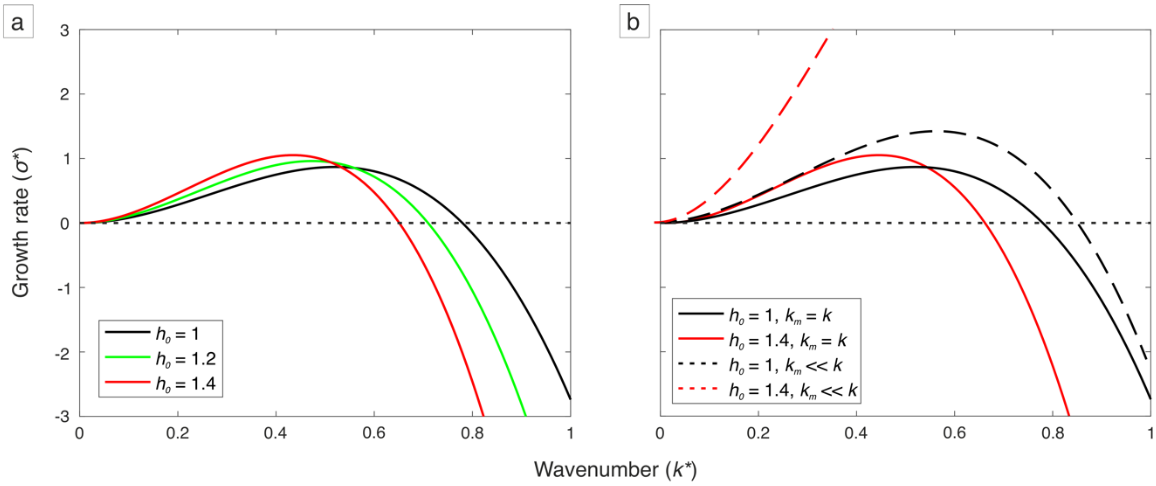

Figure S5: Normalized growth rates (σ^*) versus normalized wavenumber (k^*) plots for different values of source layer thickness (h_0) for (a) $k_m = k$, and (b) for $k_m \ll k$.